# The Role of Hydrodynamic Interaction in the Locomotion of Microorganisms

M. Ramia, D. L. Tullock, and N. Phan-Thien
From the Department of Mechanical Engineering, The University of Sydney, Sydney, New South Wales, Australia

ABSTRACT A general Boundary Element Method is presented and benchmarked with existing Slender Body Theory results and reflection solutions for the motion of spheres and slender bodies near plane boundaries. This method is used to model the swimming of a microorganism with a spherical cell body, propelled by a single rotating flagellum. The swimming of such an organism near a plane boundary, midway between two plane boundaries or in the vicinity of another similar organism, is investigated. It is found that only a small increase (less than 10%) results in the mean swimming speed of an organism swimming near and parallel to another identical organism. Similarly, only a minor propulsive advantage (again, less than 10% increase in mean swimming speed) is predicted when an organism swims very close and parallel to plane boundaries (such as a microscopic plate and (or) a coverslip, for example). This is explained in terms of the flagellar propulsive advantage derived from an increase in the ratio of the normal to tangential resistance coefficients of a slender body being offset by the apparently equally significant increase in the cell body drag. For an organism swimming normal to and toward a plane boundary, however, it is predicted that (assuming it is rotating its flagellum, relative to its cell body, with a constant angular frequency) the resulting swimming speed decreases asymptotically as the organism approaches the boundary.

## GLOSSARY

| | |
|---|---|
| $a$ | cell body radius, or radius of a given sphere |
| $a_f$ | flagellar radius, or the cross-sectional radius of a slender rod |
| $\mathbf{A}^{-1}$ | a general three-dimensional rotation matrix |
| BEM | Boundary Element Method |
| $c_r$ | common ratio for the geometric progression used to define the radial widths of the elements on the plate |
| $C$ | point defining the cell body/flagellar joining point |
| $C_t$, $C_n$, $C_b$ | tangential, normal, and bi-normal resistance coefficients for a slender rod |
| $D$, $\partial D$ | flow domain and the boundary |
| $D_T$, $D_R$ | flagellar contribution to translational and rotational drag, respectively |
| $E(z)$ | flagellar amplitude function |
| $F$ | resistive force on a sphere or slender rod/magnitude of the instantaneous flagellar propulsive force |
| $\mathbf{F}$, $\bar{F}$ | instantaneous and mean flagellar propulsive force, respectively |
| $F_i$ | magnitude of the isolated flagellar propulsive force, i.e., in the absence of cell body |
| $\mathbf{G}$, $\mathbf{H}$ | known system matrices resulting from the boundary-integral formulation |
| $h$ | separation distance defined from the center of a sphere, center of a slender rod, or an organism's cell body/flagellar joining point |
| $k_e$ | parameter determining the rate at which the flagellum grows (with axial distance) to its maximum amplitude |
| $k_f$ | flagellar wavenumber |
| $l_f$ | flagellar length or the length of a slender rod |
| $m$ | counter-variable used for reference to a given boundary element |
| $M$ | total number of quadratic elements used to discretize the boundary |
| $n$ | counter-variable used for reference to a given node |
| $n_f$ | number of longitudinal segments used to discretize the flagellar centerline |
| $n_p$ | number of radial segments used to discretize the large circular plate |
| $N$ | total number of nodes used to discretize the entire organism |
| $N_o$ | number of organisms being modeled |
| $N_{\lambda_f}$ | number of flagellar wavelengths |
| $p$ | hydrostatic pressure |
| $q$ | counter-variable used for reference to a given organism |
| $Q^{(n)}$ | shape function coefficient at the $n$th node |
| $\mathbf{r}$ | For Appendix 1, this is a position vector defining a given field point relative to a Stokeslet. Elsewhere, it is a position vector defining points on the cell body relative to the cell body $(x, y, z)$ frame |
| $\mathbf{r}_f$ | position vector defining points on the flagellum relative to the cell body $(x, y, z)$ frame |
| $\mathbf{R}$ | For Appendix 1, this is a position vector defining a given field point relative to the image of a Stokeslet. Elsewhere, it is a position vector defining points on the cell body relative to the globally fixed $(X, Y, Z)$ frame |
| $\mathbf{R}_C$ | position of the point $C$ [origin of the $(x, y, z)$ axes] relative to the globally fixed $(X, Y, Z)$ frame |
| $\mathbf{R}_f$ | position vector defining points on the flagellum relative to the globally fixed $(X, Y, Z)$ frame |
| RFT | Resistive Force Theory |
| $s_d$ | minimum separation distance |
| $s$ | normalized minimum separation distance |
| SBT | Slender Body Theory |
| $t$ | time |
| $\mathbf{t}$ | traction (local force/unit area) |
| $t^*_{ij}(\mathbf{x}, \mathbf{X})$ | traction kernel, $i$ component of traction at the field point $\mathbf{x}$ due to a Stokeslet in the $j$ direction at the point $\mathbf{X}$ |
| $T$ | resistive torque on a sphere or slender rod/magnitude of the instantaneous flagellar propulsive torque |
| $\mathbf{T}$, $\bar{T}$ | instantaneous and mean flagellar propulsive torque, respectively |

*Received for publication 18 September 1992 and in final form 29 March 1993.*

Address reprint requests to Dr. Marcel Ramia.



0006-3495/93/08/755/24 $2.00

| | |
|---|---|
| $T_i$ | magnitude of the isolated flagellar propulsive torque, i.e., in the absence of cell body |
| $\mathbf{u}$ | velocity vector |
| $u_{ij}^*(\mathbf{x}, \mathbf{X})$ | velocity kernel, $i$ component of velocity at the field point $\mathbf{x}$ due to a Stokeslet in the $j$ direction at the point $\mathbf{X}$ |
| $\mathbf{U}$ | instantaneous swimming velocity |
| $U$ | translational velocity of a sphere or slender rod |
| $\bar{U}$ | mean swimming speed |
| $\nu_f$ | number of sides on the polygon used to discretize any given cross-section of flagellum |
| $\nu_p$ | number of angular segments used to discretize the large circular plate |
| $\mathbf{W}$ | three-dimensional rotation matrix |
| $\mathbf{x}$ | coordinates of a typical point in the flow domain |
| $\mathbf{X}$ | coordinates of a point where a Stokeslet is situated |
| $\mathbf{X}^*$ | coordinates of a point where the image system to a Stokeslet is situated. This is the reflection of the point $\mathbf{X}$ about the half-space. |
| $(x, y, z)$ | axes defining a frame at rest with respect to the cell body (i.e., flagellar frame) |
| $(X, Y, Z)$ | axes defining the globally fixed frame of reference |
| $z_e$ | axial extension of the flagellar end region |
| $z_m$ | maximum axial extension of the flagellum |
| $\alpha_f$ | flagellar amplitude |
| $\gamma_1, \gamma_2$ | ratio of normal to tangential, and bi-normal to tangential resistance coefficients for a slender rod, respectively |
| $\delta_{ij}$ | Kronecker delta |
| $\Delta\theta$ | relative flagellar phase angle between two organisms that are close and parallel to each other |
| $\Delta F, \Delta T$ | the change in the magnitude of the flagellar propulsive force and torque due to the cell body/flagellar hydrodynamic interaction, respectively |
| $\Delta t$ | small but finite time increment |
| $\mu$ | fluid viscosity |
| $\theta$ | flagellar phase angle $\omega t$ |
| $\psi_1, \psi_2, \psi_3$ | Euler angles |
| $\phi$ | angle of the flagellar axis relative to the half-space |
| $\lambda_f$ | flagellar wavelength |
| $\omega$ | magnitude of the angular velocity of the flagellum, relative to the cell body (same for all organisms) |
| $\Omega$ | angular velocity of a sphere |
| $\boldsymbol{\omega}_{q+1}$ | angular velocity of the cell body, relative to the flagellum, for organism $q$ |
| $\boldsymbol{\Omega}_q$ | instantaneous angular velocity of the cell body belonging to organism $q$ |
| $\boldsymbol{\Omega}_{q+1}$ | instantaneous angular velocity of the flagellum belonging to organism $q$ |
| $\bar{\Omega}$ | mean angular velocity of a given organism |
| $\infty$ | usual infinity sign, used as subscript to denote the values of the given quantities in an unbounded fluid |

## INTRODUCTION

It is generally accepted that bacteria propel themselves through fluids by rotating a flagellum or a flagellar bundle (several flagellar filaments that rotate together as a single unit) (1). A recent study has been made of the molecular rotary motor that rotates each filament (relative to the cell body) at its base (2). The manner in which an organism swims is largely determined by the speed and direction of rotation of such motors. The control mechanisms of these motors in turn are sensitive to variations in many factors such as light intensity, fluid temperature, and perhaps, more importantly, fluid chemistry. The mechanism by which an organism moves or alters its motion in response to a chemical stimulus is referred to as *chemotaxis* and has been studied extensively. Stewart and Dahlquist (3) give a review of the biochemical aspects of chemotaxis, and Berg and Turner (4) investigate its effects on the motility of *Escherichia coli*. Crenshaw (5, 6) and Crenshaw and Edelstein-Keshet (7) propose that microorganisms can reorientate themselves in response to a chemical or other stimulus by changing the direction of their rotational velocity.

As bacteria respond to some of the above-mentioned factors, they are often subjected to swimming in close proximity to each other as well as other boundaries. The resulting hydrodynamic interactions may have puzzling effects on their swimming speed, trajectory, and power dissipation. For example, Baba et al. (8) express concern about the effects of container walls on their experimental measurements of swimming paths. Myerscough and Swan (9) attribute a poor correlation between their model predictions and experimental observations of mean swimming speeds to the presence of a microscopic plate and coverslip. Berg and Turner (4) observed that when *E. coli* swims very close and parallel to a plane boundary, it tends to swim in spirals rather than straight lines. The current understanding of this subject is largely incomplete; it is based on superposing existing knowledge of the behavior of spheres and that of slender bodies near walls (or near other particles) to model the likely behavior of microorganisms, which are assemblies of such particles. It is the aim of the present study to further elucidate such models.

The flow associated with flagellar propulsion is inertialess, incompressible, and highly viscous. Therefore, it is governed by the Stokes equations (see Brennen and Winet (10)) subject to the "no-slip" boundary conditions on the flagellar surface and the vanishing fluid disturbance at infinity (i.e., on the boundary, the fluid velocity must match the velocity of the boundary, and far away from this boundary, the fluid velocity must approach zero). Direct analytical solution of these equations is possible, but only if some simplifying assumptions regarding the flow geometry and boundary conditions are made. Alternatively, there are several well-known fundamental singular solutions, such as Stokeslets (point forces) and doublets (sources and sinks that are made to coincide), the induced velocity fields of which vanish at infinity. Due to the linearity of the governing equations, the superposition of any number of these singularities results in velocity fields that also vanish at infinity. There are at least two acceptable approaches in which these singularities may be utilized to model flagellar propulsion, namely, Slender Body Theory (SBT) and Resistive Force Theory (RFT, which is ultimately based on SBT). The present study, however, is concerned with the somewhat different approach of the Boundary Element Method (BEM).

The study of flagellar propulsion by direct solution of the governing equations was carried out by Taylor (11). Here, the flagellum was modeled as an infinite cylindrical filament executing small-amplitude waves (compared with its cross-sectional radius) in an unbounded fluid. Generalizations of this approach to model hydrodynamic interaction between neighboring flagella or with solid boundaries were all restricted to unrealistic two-dimensional flows. Taylor (12) represented such flagella by infinite waving thin sheets and concluded that if two neighboring flagellar waves are beating in phase with each other, very much less energy is dissipated than if they were beating out of phase. Furthermore, if these waves are initially out of phase, the fluid tends to force them back into phase. Reynolds (13) extended this idea to model a flagellum in the vicinity of a solid boundary (see also Blake (14) and Smeltzer (15)). Like previous analyses, this utilized the assumption of small-amplitude waves to apply boundary conditions expanded about the mean planes of the wavy sheets. Katz (16) also developed a model using an infinite waving sheet near and parallel to a single wall or at an arbitrary position between and parallel to two such walls. He employed a combination of lubrication theory (see O'Brien (17)), when the sheet is very close to a wall (i.e., a separation distance of the same order as the wave amplitude), and biharmonic analysis (i.e., direct solution), when the sheet is very far from a wall. An increase in the propulsive velocity, at the expense of an associated increase in power as the given wall separation distances decrease, was predicted.

Hancock (18) considered the superposition of a line distribution of Stokeslets and doublets along the flagellar centerline. By imposing the no-slip boundary conditions on the flagellar surface, the strengths of these singularities were determined. Then, the flagellar propulsive force was calculated and equated to the cell body drag, giving an estimate of the swimming velocity. In a similar manner the propulsive torque may be calculated, giving an estimate of the organism's counter-rotational angular velocity (however, this was not carried out by Hancock (18)). This technique is generally applicable to bodies whose curvature and cross-sectional dimensions are small, compared with their lengths, and became known as SBT. Many subsequent models were based on this overall approach, and a review of some of these may be found in Brennen and Winet (10).

Higdon (19–21) developed an improved SBT in which the Stokes equations were transformed into a system of singular integral equations in terms of the swimming velocity, angular velocity, and the variable singularity strength along the flagellar centerline. Image systems for the singularities were included at the cell body center and behind a zero-displacement plane boundary, thereby simultaneously accounting for the presence of a cell body and a neighboring wall. Arbitrary flagellar beats and centerline geometries were also allowed, and applications such as the propulsion of a microorganism by sinusoidal (planar) as well as by helical flagellar rotation were included. In addition, feeding currents (set up by an organism, for the purposes of feeding, when it attaches itself to a substrate via a stalk) were also studied and showed good agreement with experimental observations (see Lapage (22) and Sleigh (23), for example). Although this method had the potential to correctly model the swimming near a single wall, it was never applied to such a task. However, it was only applicable to spherical cell bodies and slender flagella. But more importantly, modeling the swimming of an organism near other organisms or between two walls was not possible.

Further examples of the application of SBT to account for hydrodynamic interactions may be found. Myerscough and Swan (9) modeled the swimming of a *Spirillum volutans* and compared the calculated predictions with their own experimental observations of mean swimming speeds. The agreement was not good, because the slender body assumption restricted the geometrical representation of the organism to somewhat unrealistically thin cell bodies. Gueron and Liron (24) modeled the beat coordination (metachronism) of cilia attached to the epithelium of a microorganism (on a local scale, this is essentially a solid plane wall). They postulated that hydrodynamic interaction between neighboring cilia plays an important role in the metachronism phenomenon (see Brennen and Winet (10), or the more recent Sleigh et al. (25), for reviews on ciliary motion).

Gray and Hancock (26) proposed that each elemental length of the flagellum experiences a resistive force that is proportional to the difference between the fluid velocity and the local flagellar velocity. For the case when this elemental length is moving in a direction parallel to its centerline, the constant of proportionality ($C_t$) is said to be the tangential resistance coefficient. A similar definition follows for $C_n$, the normal resistance coefficient. Although both of these coefficients will vary slightly along the length of the flagellum, they are presumed constant for a given flagellar waveform and cross-sectional radius. Expressions for these coefficients were derived from SBT (see Lighthill (27), for example). Here, the effect of the fluid is replaced by such coefficients, and appropriate integrations of the resulting elemental resistive forces, along the entire length of the flagellum, yield both the propulsive force and torque. These may be compared with the translational and rotational drag on the cell body, giving the swimming velocity and counter-rotation angular velocity. This approach became known as RFT and was applied by Gray and Hancock (26) to model the propulsion of sea urchin spermatozoa, which execute planar sinusoidal flagellar waves. Later, Chwang and Wu (28) (see also Shreiner (29)) applied the same technique to model organisms propelled by helical flagellar rotation.

Generalization of the above RFT approach to modeling more complex situations involved the use of modified resistance coefficients. For example, modifications may account for the presence of a wall (see The Motion of a Slender Body Near Plane Boundaries, below) or a cell body (see Lighthill (27)). Katz and Blake (30) applied the modified coefficients of Katz et al. (31) to investigate the effects of nearby walls on the propulsive force and power dissipation of a flagellum. They showed that the propulsive force is heavily dependent on, and increases with, the ratio of normal

to tangential resistance coefficients. The power dissipation, on the other hand, increases independently with each of these coefficients. It was mentioned that these predictions may be compared with the expected increase in the cell body drag to arrive at a resulting swimming speed. This was not carried out, however, even though estimates of the cell body drag near a wall, or between two such walls, were in existence at the time (Wakiya (32), and Happel and Brenner (33)). This approach presupposes small-amplitude flagellar waves, and the coefficients used were valid only when the flagellum is very close to the wall. Hence, their results were at best qualitative.

Phan-Thien et al. (34) applied the BEM to study the locomotion of a microorganism propelled by helical flagellar rotation. They determined the optimal geometrical parameters that allow the organism to attain a maximum swimming speed for a given power dissipation. These optimal parameters showed excellent agreement with those of the SBT model of Higdon (21), which in turn agreed qualitatively with experimental observation of efficiently swimming microorganisms (see, for example, Rikmenspoel (35) and Leifson (36)). Ramia (37) carried out a similar BEM study of the optimal locomotion of the *S. volutans*. Because the cell body of this organism (which has a helical shape) is not very "slender," the BEM results showed considerably better agreement with the experimental observation of Myerscough and Swan (9) than their own SBT model.

In the present study, a general BEM is presented and benchmarked with existing SBT results (and reflection solutions) for the motion of spheres and slender bodies near plane boundaries. This method is applicable to any number of organisms, each of which may have any arbitrary geometry, orientation, and distance from a given plane boundary. However, only results relating to a uniflagellated, spherical microorganism (with typical dimensions and proportions) propelled by helical flagellar rotation are included. The swimming of this organism parallel to and midway between two parallel walls, near and parallel to another identical organism, or at an arbitrary orientation to and near a single wall, is considered.

## BOUNDARY ELEMENT METHOD

The BEM has been successfully applied to Stokes flow problems by Youngren and Acrivos (38), Bush and Tanner (39), and Tran-Cong and Phan-Thien (40). Here, this method will be briefly outlined, but a more comprehensive review may be found in Kim and Karrila (41). The Stokes equations may be expressed as

$$\mu\nabla^2\mathbf{u} = \nabla p, \qquad \nabla\cdot\mathbf{u} = 0, \qquad \mathbf{x}\in D \tag{1}$$

where $\mathbf{u}$ is the velocity vector, $p$ is the hydrostatic pressure, $\mu$ is the viscosity of the fluid, and $D$ is the flow domain. These may be expressed as boundary integral equations in terms of the velocity field by the use of Betti's Reciprocal Work Theorem (see Banerjee and Butterfield (42), Brebbia et al. (43), or Kim and Karrila (41)):

$$c_{ij}(\mathbf{x})u_j(\mathbf{x}) = \int_{\partial D} u^*_{ij}(\mathbf{x},\mathbf{X})\, t_j(\mathbf{X})\, dS(\mathbf{X}) - \int_{\partial D} t^*_{ij}(\mathbf{x},\mathbf{X})u_j(\mathbf{X})\, dS(\mathbf{X}), \tag{2}$$

where $\partial D$ is the Liapunov smooth boundary of the solution domain $D$, $\mathbf{X}\in\partial D$, $u_j(\mathbf{X})$ is the $j$ component of the velocity at $\mathbf{X}$, $t_j(\mathbf{X})$ is the $j$ component of the boundary traction at $\mathbf{X}$, $u^*_{ij}(\mathbf{x}, X)$ is the $i$ component of velocity field at $\mathbf{x}$ due to a Stokeslet in the $j$ direction at $\mathbf{X}$, and $t^*_{ij}(\mathbf{x}, \mathbf{X})$ is its associated traction (see Fig. 1). Here, $c_{ij}(\mathbf{x})$ depends upon the location of $\mathbf{x}$ and the local geometry; it is given by

$$c_{ij} = \begin{cases} \tfrac{1}{2}\delta_{ij} & \mathbf{x}\in\partial D \text{ smooth at } \mathbf{x} \\ \delta_{ij} & \mathbf{x}\in D \\ 0 & \mathbf{x}\notin D \end{cases}$$

Expressions for $u^*_{ij}(\mathbf{x}, \mathbf{X})$ and $t^*_{ij}(\mathbf{x}, \mathbf{X})$ depend on whether the flow domain $D$ is an unbounded fluid or a half-space due to the presence of a zero-displacement boundary and are discussed in Appendix 1.

For a boundary discretized into $M$ elements over which the boundary solution is approximated by a piecewise continuous polynomial (for example, the velocity over an element may be given by $u_j = Q^{(n)}u_j^{(n)}$), Eq. 2 becomes

$$c_{ij}(\mathbf{x})u_j(\mathbf{x}) = \sum_{m=1}^{M}\left(u_j^{(n)}\int_{\partial D_m} u^*_{ij}(\mathbf{x},\mathbf{X})Q^{(n)}\, dS(\mathbf{X}) - t_j^{(n)}\int_{\partial D_m} t^*_{ij}(\mathbf{x},\mathbf{X})Q^{(n)}\, dS(\mathbf{X})\right), \tag{3}$$

where $n$ refers to a given node, $m$ refers to a given element, $Q^{(n)}$ (with $n$ varied through all nodes defining the element $m$) represents the shape function, and summation is implied by the multiple occurrence of $n$. This equation, when applied to a series of collocation points (usually, but not necessarily the nodal points) over the boundary, leads to a set of linear algebraic equations. Gaussian elimination may then be used to solve these equations, given appropriate traction and (or) velocity boundary conditions.

The boundary $\partial D$ is discretized into a combination of 6-noded trilateral and 8-noded quadrilateral elements. The functional variation (of either velocity or traction) on the elements may be of the same order as the geometry (namely quadratic), resulting in the so-called isoparametric elements, or of a smaller order, resulting in the so-called superparametric elements (Bathe (44)).

### The motion of a sphere near plane boundaries

Lee and Leal (45) gave an exact solution to the problem of a sphere translating or rotating in the vicinity of a fluid-fluid interface (with different viscosities). Of particular interest here are the results relating to the motion of a sphere near a

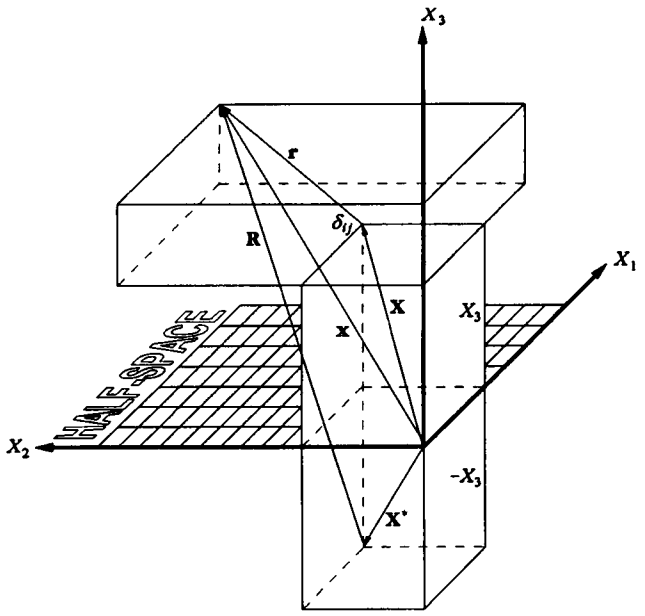


FIGURE 1 Definition of variables associated with the unbounded and half-space kernels.

solid plane boundary (which hereafter may be referred to as a wall or a half-space). These results have since been used, and are used here, for benchmarking purposes (see Tran-Cong and Phan-Thien (46) and Phan-Thien et al. (47)). Wakiya (32) studied the problem of a sphere translating parallel to and between two parallel walls (which hereafter may be referred to as parallel plates). This was based on the so-called method of reflections, originally developed by Smoluchowski (48) (see also Faxén (49) and Happel and Byrne (50)). His results were not valid for a sphere very close to either wall, namely, for a normalized separation distance ($h/a$) less than 2 (as defined in Fig. 3 *b*).

Ordinarily, in the BEM the presence of a half-space is accounted for by modification of the velocity and traction kernels (as in Appendix 1; see also Tran-Cong and Phan-Thien (46)). An alternative, but computationally more expensive approach would be to have a large discretized plate modeling the half-space. For ease of numerical calculation, this plate is discretized into a closed flat circular disk having a small but finite thickness ($\approx$ 1% of the plate radius, for example). Much like a half-space, the velocity boundary conditions are set to zero for all nodes on the side of the plate facing the given organism or other body (i.e., facing what may be termed the "flow domain"), and the unspecified tractions on these nodes are later determined as part of the solution process. As shown in Fig. 3 *a*, both the velocity and traction boundary conditions are set to zero for nodes lying on the other side of the plate (i.e., not facing the "flow domain"), and hence such nodes do not contribute to the size of the problem while allowing the plate to be treated numerically as a closed body.

Modeling a half-space via a finite discretized plate would introduce two sources of error, one due to the finite size of the plate and the other to the plate discretization. Both of these errors are maintained at acceptably small values by ensuring that the plate is much larger than the body being modeled and that a finer local discretization of the plate is

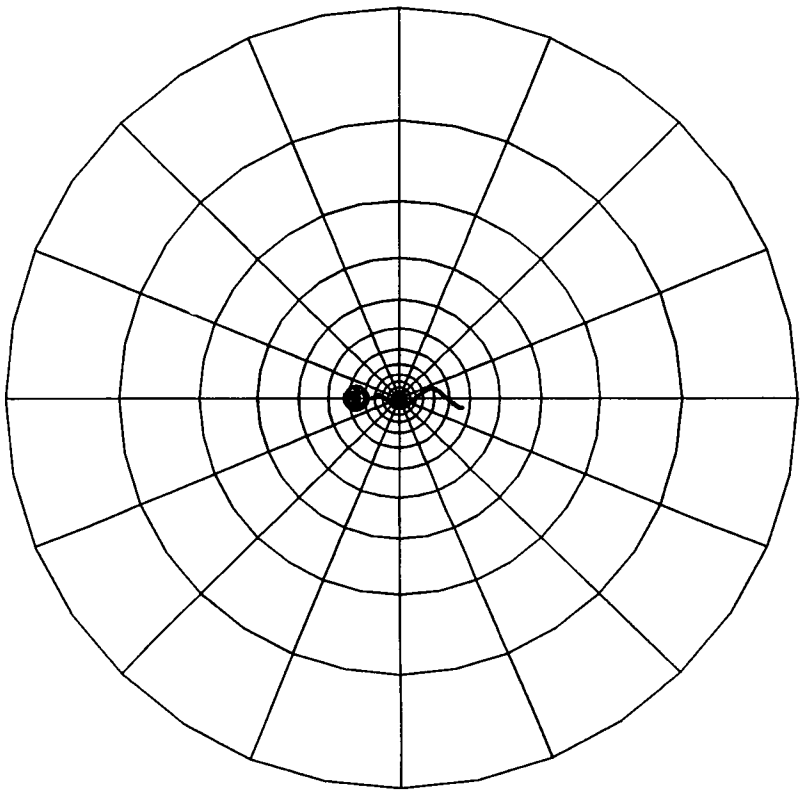

FIGURE 2 Top view of the large circular plate (used to model a half-space), showing its size and discretization relative to those of the organism.

used where this body is closest to the plate (see Fig. 2, which shows a typical plate discretization). Here, a plate radius of 15 is used throughout, while the sphere radius is maintained constant at 1. A combination of such a plate and a half-space is used to model the motion of spheres and slender bodies, as well as the locomotion of microorganisms between two parallel plates. This type of approach is necessary, since a relevant closed-form BEM kernel cannot be found.

Fig. 3 *c* shows the force on a sphere translating parallel to a half-space as a function of the normalized separation distance ($h/a$). Results due to the BEM with a half-space kernel, the BEM with a large discretized plate, and the exact solution of Lee and Leal (45) are included. These have all been normalized with respect to $F_\infty = 6\pi\mu aU$ (where $U$ is the specified translational velocity; see Happel and Brenner (33)), the drag on a translating sphere in an unbounded fluid. Very good agreement among all three is apparent. Furthermore, the two BEM results agree to the fourth decimal place, and typically

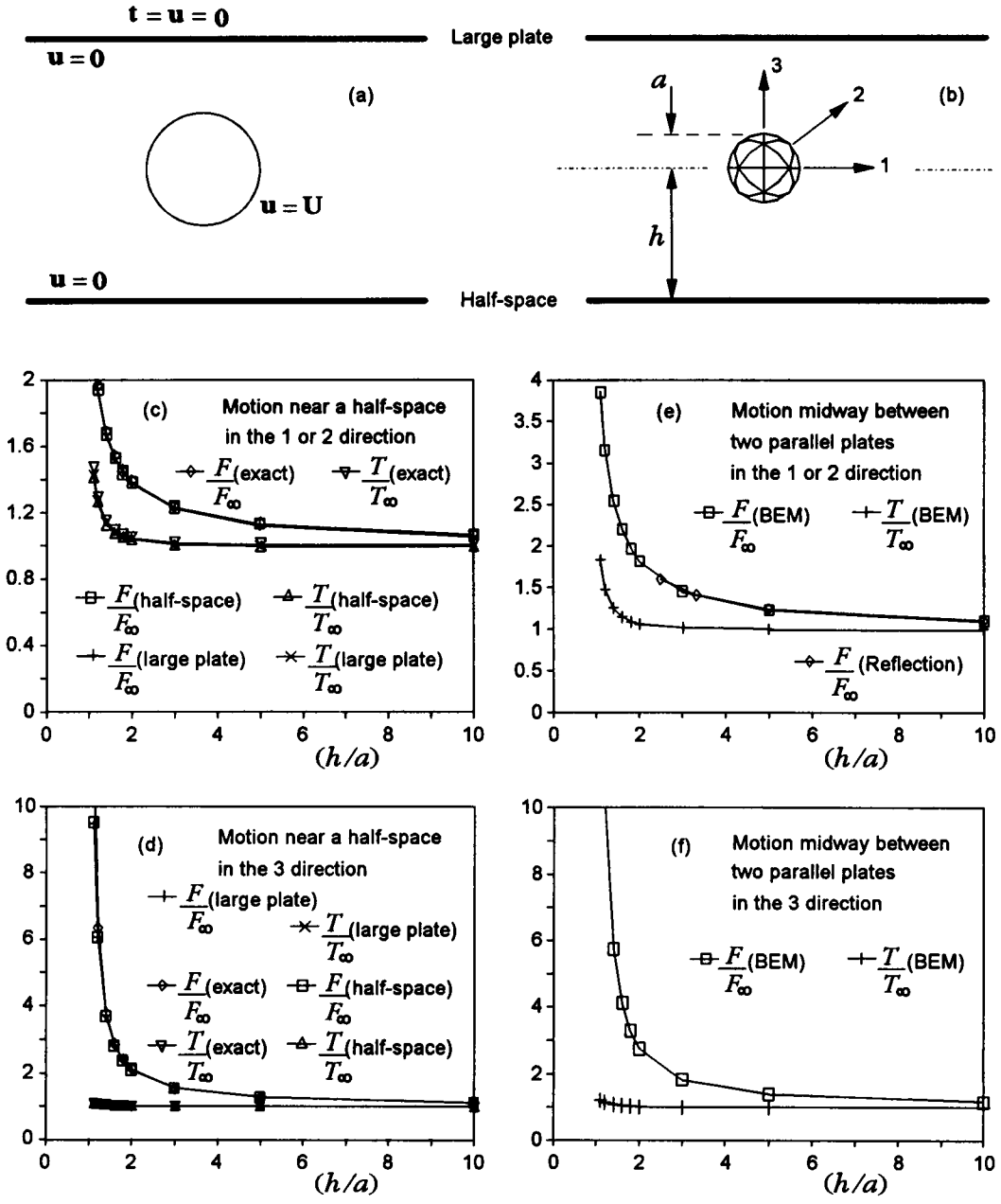


FIGURE 3 Results relating to the motion of a sphere near a half-space or midway between two parallel plates. (*a*) Description of the relevant boundary conditions. (*b*) Definition of the directions of motion and separation distance. (*c*) For a sphere translating parallel to a half-space, or rotation about an axis which is parallel to this half-space, graphs of normalized force $F/F_\infty$ and torque $T/T_\infty$ versus the normalized separation distance ($h/a$), as calculated by the BEM with a half-space kernel, as calculated by the BEM using a large discretized plate, or as given by Lee and Leal's (45) exact solution. (*d*) As for (*c*), except that it relates to translation in a normal direction, or rotation about a normal axis. (*e*) As for (*c*), except that it relates to motion between two parallel plates, and only the BEM results and those of Wakiya (32) are included. (*f*) As for (*d*), except that it relates to motion between two parallel plates, and only the BEM results are included.

there is 0.5% error between these results and the exact solution. This error rises to about 1% as the sphere becomes very close to the wall (i.e., for $(h/a) \approx 1.1$). A similar trend follows for the torques, which have been normalized with respect to $T_\infty = 8\pi\mu a^3\Omega$ (where $\Omega$ is the specified angular velocity; again see Happel and Brenner (33)), the torque on a rotating sphere in an unbounded fluid. For motions in the normal direction, considered in Fig. 3 *d*, the error in drag is less than 1% for $(h/a) > 1.4$ but rises very steeply to exceed 15% for $(h/a) \approx 1.1$. This is to be expected, given the somewhat asymptotically sharp rise in drag as the sphere approaches the rigid boundary. On the whole, two conclusions may be drawn from these results. First, a large discretized plate can be used to accurately model the effect of a half-space. Second, the constant curvature of a sphere is very efficiently modeled by the quadratic elements. For example, the present discretization involving 198 unknowns (3 times the number of collocation points, here 66) yields 0.3% error in the drag on a sphere in an unbounded fluid. This compares favorably with an error of 1.3% for the same problem with 240 unknowns (80 constant elements) reported by Phan-Thien et al. (34).

Fig. 3 (*e* and *f*) shows the normalized forces and torques for a sphere moving midway between two parallel plates. For the case of parallel translation, there is good agreement with the reflection solution results of Wakiya (32), within their reported range of validity. Much like the case of motion near a half-space, the general trend is an increase in torque and a more severe increase in force as the wall separation distances decrease. As intuitively expected, both the force and torque, for a given separation distance, are larger for a sphere between two walls than they are for a sphere near a single wall.

### The motion of a slender body near plane boundaries

Brenner (51) derived a general expression giving the modified resistance coefficients for an arbitrary body due to the presence of a wall or midway between two such walls. However, this expression was valid only when the body is situated at a distance from the wall (or walls) that is large compared with its own dimensions. This restriction is particularly limiting for the case of a long slender rod. Katz et al. (31) considered the resistance coefficients for such a rod oriented parallel to a single wall or midway between two walls. Their results were valid for separation distances that are small compared with the rod's length and large compared with the rod's cross-sectional radius. SBT (as developed by Tillet (52) and Cox (53)) was employed for the single wall case and the method of reflections for that of two parallel walls. All of these studies exhibited the same general trends. Namely, each of the resistance coefficients, as well as the ratio of normal to tangential coefficients, increased as the slender rod approached the wall.

De Mestre (54) and de Mestre and Russel (55) examined the effects of a single wall on the motion of slender rods having either orientation (i.e., parallel or perpendicular) relative to and arbitrary separation distances from such a wall. The relevant particular cases of their results converge asymptotically to those of Brenner's (51) for large separation distances and to those of Katz et al. (31) for small distances. Fulford and Blake (56, 57) studied the motion of slender rods in the vicinity of a fluid-fluid interface. A general viscosity ratio was allowed for the two immiscible fluids, thereby modeling the full range of interfaces from a zero-traction free surface to a zero-displacement boundary. In particular, they were interested in a viscosity ratio of $\approx 10^3$, which represents the relevant fluid-fluid interface for modeling mucociliary transport (see Sleigh et al. (25)). They showed that, for the special case of an infinite viscosity ratio (i.e., a zero displacement boundary), their results are in full agreement with those of de Mestre and Russel (55). This is to be expected, since they were based on essentially the same SBT. However, both Brennen and Winet (10) as well as Fulford and Blake (56) warn of serious typographical errors in the results of de Mestre and Russel (55).

Fig. 4 shows the tangential resistance coefficient $C_t/C_{t\infty}$ (normalized with respect to its value in an unbounded fluid), the ratio of normal to tangential resistance coefficient $\gamma_1 = C_n/C_t$, and the ratio of the bi-normal to the tangential resistance coefficient $\gamma_2 = C_b/C_t$ (where applicable) as functions of the normalized separation distance ($(h/2l_f)$ for parallel orientation and $(h - l_f)/2l_f$ for normal orientation) for a slender rod of length $2l_f$ translating near a half-space or midway between two plates. Details of the rod's dimensions and discretization are given in Appendix 2. For motion near a half-space, the present BEM results (Fig. 4, *c* and *d*) show generally good agreement with the SBT results of Fulford and Blake (56), the only exception being that for perpendicular orientation, very close to a half-space. This is to be expected, given that Fulford and Blake (56) presumed separation distances greater than several rod cross-sectional radii.

Fig. 4 *e* shows the results relating to the motion of a rod parallel to and midway between two parallel plates. The above-mentioned limited range of validity of the results of Katz et al. (31), together with the fact that both $C_t$ and $\gamma_1$ rise sharply, in this range, renders a direct comparison with the present BEM results infeasible.

## THE MODEL

Based on previous models, such as that of Higdon (21), the geometry of the organism is modeled in a manner allowing variations in any of the geometrical parameters. A global resistance matrix is set up (see Happel and Brenner (33)), which together with equilibrium considerations enables the calculation of the instantaneous swimming velocity and counter-rotation angular velocity. The mean swimming speed is determined from a predicted swimming trajectory as outlined under Approximate Kinetics Scheme and Organism Tracking Scheme, below. This and other mean quantities are normalized with respect to their corresponding values in an unbounded fluid and plotted as functions of the relevant separation distances (from the given boundaries or other organisms).

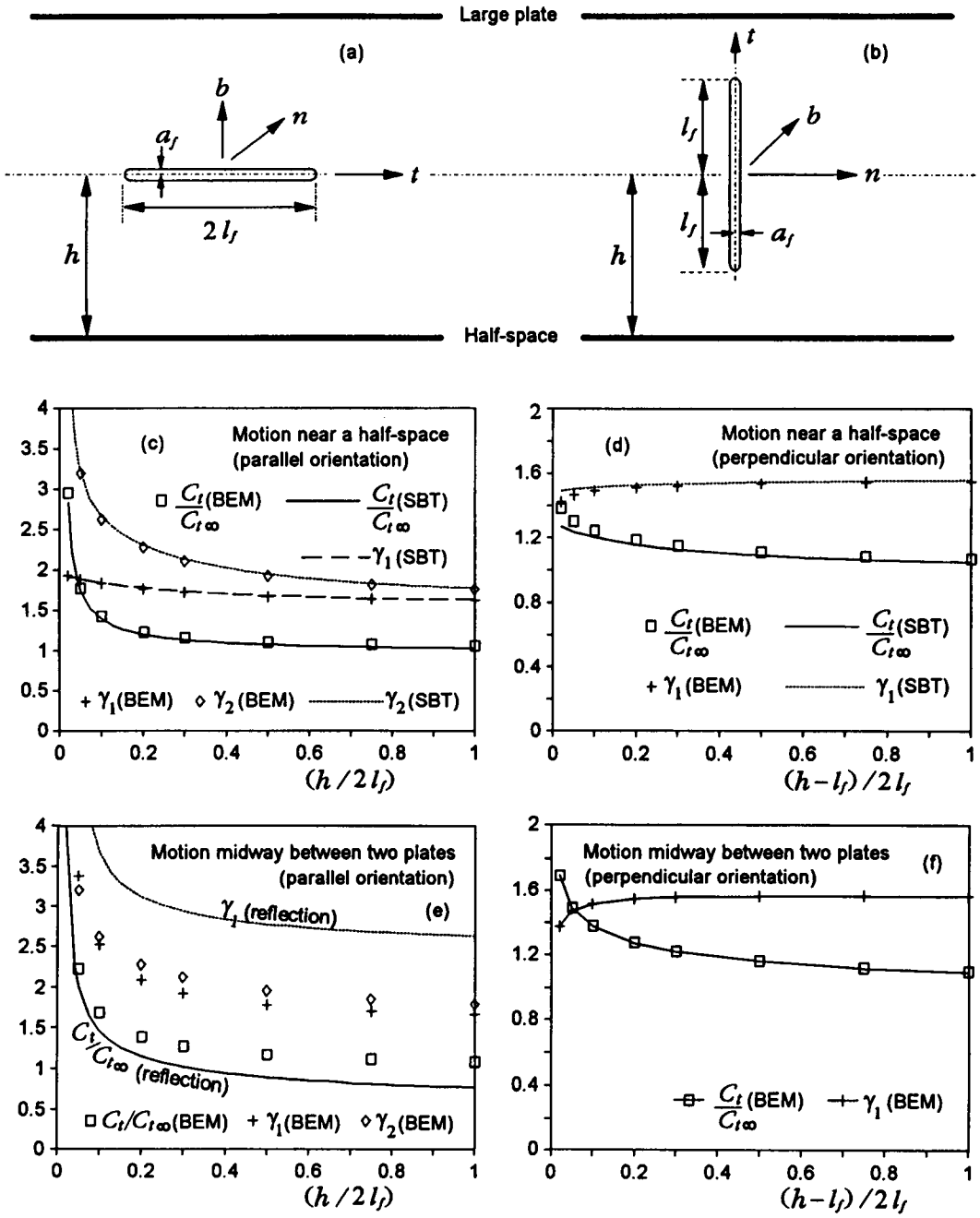


FIGURE 4 Results relating to the motion of a slender rod, with either parallel or perpendicular orientation, near a half-space or midway between two parallel plates. (*a*) For a slender rod with parallel orientation; definition of rod dimensions, separation distance, as well as the tangential, normal, and bi-normal directions. (*b*) For a slender rod with perpendicular orientation; otherwise as for (*a*). (*c*) For the case of a slender rod parallel to and near a half-space, graphs of the normalized tangential resistance coefficient $C_t/C_\infty$, ratio of normal to tangential resistance coefficients $\gamma_1 = C_n/C_t$, and ratio of bi-normal to tangential resistance coefficients $\gamma_2 = C_b/C_t$ versus the normalized separation distance $(h/2l_f)$ (both the present BEM results and the SBT results of Fulford and Blake (56, 57) are included). (*d*) As for (*c*), except that it relates to a rod with perpendicular orientation; here $\gamma_1 = \gamma_2$, and the normalized separation distance is taken to be $(h - l_f)/2l_f$. (*e*) As for (*c*), except that it relates to a slender rod parallel to and midway between two parallel plates (both the present BEM results and the relevant reflection solution results of Katz et al. (31) are included). (*f*) As for (*c*), except that it relates to a slender rod perpendicular to and midway between two parallel plates (only the present BEM results are included, and again, the normalized separation distance is taken to be $(h - l_f)/2l_f$).

## Geometrical modeling

The geometry of a microorganism with a spherical body and a single helical flagellum is as shown in Fig. 5. The position vector $\mathbf{r}_f$, defining the flagellar centerline as a function of time $t$ relative to the $(x, y, z)$ frame of reference, which is at rest with respect to the cell body, may best be approximated by (see Higdon (21))

$$\mathbf{r}_f = [\alpha_f E(z)\cos(k_f z - \omega t), \alpha_f E(z)\sin(k_f z - \omega t), z]$$

$$E(z) = 1 - \exp[-(k_e z)^2], \qquad 0 \le z \le z_m \tag{4}$$

which is a right-handed helix of maximum amplitude $\alpha_f$,

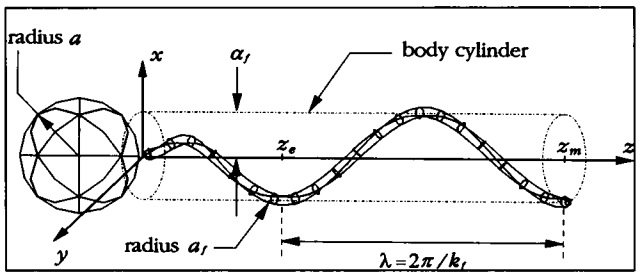


FIGURE 5 Definition of the organism's geometrical parameters (the discretization used is also shown).

wavenumber $k_f$, and axial length $z_m$ (see Fig. 5). The amplitude function $E(z)$ grows to ≈98% of its maximum value of 1 within the end region, whose extent $z_e$ is determined by the parameter $k_e$ (i.e., $z_e = 2/k_e$). The cell body is then modeled as a sphere of radius $a$ centered at $(0, 0, -a)$, whereby the joining point $C$ is located at the origin (refer to Appendix 2 for a discussion of the discretization scheme).

The flagellar phase angle is $\theta = \omega t$, where $\omega$ is the presumed constant magnitude of the angular velocity of the flagellum relative to the cell body about the flagellar axis (i.e., the $z$-axis). The position vector (relative to the $(x, y, z)$ frame) of any given point on the surface of the flagellum (at any time $t$), which has an assumed constant circular cross-sectional radius $a_f$, depends upon the type of flagellar rotation (or waveform) in question. Microorganisms such as spermatozoa, which may swim by executing three-dimensional bending "helical" flagellar waves, are said to possess eukaryotic flagella that have the same structure as cilia (Brennen and Winet (10)). Bacteria, on the other hand, are said to have prokaryotic flagella and generally swim by rotating these flagellar filaments (Meister et al. (2)). From a simplified modeling point of view, for a given centerline waveform such as that described by Eq. 4, the difference between eukaryotic and prokaryotic flagella rotation, in terms of the flagellar surface kinematics, is a minor one because the radius $a_f$ is small compared with the flagellar amplitude. This difference is particularly insignificant in the present study, where the emphasis is on the effects due to the presence of boundaries rather than on swimming in an unbounded fluid. Hence, throughout this study, the flagellum is assumed to rotate as a rigid body (with a constant angular velocity) relative to the cell body.

The following proportions for the organism (in dimensionless form) are used as default values in the present calculations:

$$\alpha_f k_f = 1, \qquad \frac{k_f}{k_e} = 1, \qquad N_{\lambda_f} = 1.5,$$

$$\frac{l_f}{a} = 10, \qquad \text{and} \qquad \frac{a_f}{a} = 0.1$$

where $N_{\lambda_f}$ is the number of helical wavelengths and $l_f$ is the numerically calculated flagellar length (the relevant resulting organism is as shown in Fig. 5). These particular values are typical of what is observed experimentally (see, for example, Tables 3, 4, and 5 in Brennen and Winnet (10)) and were deduced by both Higdon (21) and Phan-Thien et al. (34) to be the optimal dimensions and proportions of the organism; hence they were adopted here.

## Instantaneous velocities

Consider $N_o$ organisms, for each of which the flagellum and the cell body are each treated as separate, individual bodies (i.e., closed surface). This is made possible by maintaining a small but finite separation distance $a_f/2$ between the cell body and flagellum (see Appendix 4 for a more detailed treatment). The viscous force $\mathbf{F}$ and torque $\mathbf{T}$ acting on a typical surface $S_k$ are given by the integrals

$$\mathbf{F} = \oint_{S_k} \mathbf{t}\, dS \qquad \text{and} \qquad \mathbf{T} = \oint_{S_k} (\mathbf{x} \times \mathbf{t})\, dS \qquad (5)$$

where $\mathbf{t}$ is the traction on the boundary $S_k$, and $\mathbf{x}$ represents the displacement vector from the cell body/flagellar joining point $C$.

Using the boundary element method to solve for the boundary traction and Eq. 5, a series of $12N_o$ numerical experiments may be carried out, enabling the calculation of the elements composing the resistance matrix in the following equation (Happel and Brenner (33)):

$$\begin{pmatrix} \mathbf{F}_1 \\ \mathbf{T}_1 \\ \mathbf{F}_2 \\ \mathbf{T}_2 \\ \vdots \\ \mathbf{F}_{N_o} \\ \mathbf{T}_{N_o} \end{pmatrix} = \begin{pmatrix} \mathbf{K}_{11} & \mathbf{L}_{11}^T & \mathbf{K}_{12} & \mathbf{L}_{12}^T & \cdots & \mathbf{K}_{1N_o} & \mathbf{L}_{1N_o}^T \\ \mathbf{L}_{11} & \mathbf{M}_{11} & \mathbf{L}_{12} & \mathbf{M}_{12} & \cdots & \mathbf{L}_{1N_o} & \mathbf{M}_{1N_o} \\ \mathbf{K}_{21} & \mathbf{L}_{21}^T & \mathbf{K}_{22} & \mathbf{L}_{22}^T & \cdots & \mathbf{K}_{2N_o} & \mathbf{L}_{2N_o}^T \\ \mathbf{L}_{21} & \mathbf{M}_{21} & \mathbf{L}_{22} & \mathbf{M}_{22} & \cdots & \mathbf{L}_{2N_o} & \mathbf{M}_{2N_o} \\ \vdots & \vdots & \vdots & \vdots & \cdots & \vdots & \vdots \\ \mathbf{K}_{N_o1} & \mathbf{L}_{N_o1}^T & \mathbf{K}_{N_o2} & \mathbf{L}_{N_o}^T & \cdots & \mathbf{K}_{N_oN_o} & \mathbf{L}_{N_oN_o}^T \\ \mathbf{L}_{N_o1} & \mathbf{M}_{N_o1} & \mathbf{L}_{N_o2} & \mathbf{M}_{N_o2} & \cdots & \mathbf{L}_{N_oN_o} & \mathbf{M}_{N_oN_o} \end{pmatrix} \begin{pmatrix} \mathbf{U}_1 \\ \boldsymbol{\Omega}_1 \\ \mathbf{U}_2 \\ \boldsymbol{\Omega}_2 \\ \vdots \\ \mathbf{U}_{N_o} \\ \boldsymbol{\Omega}_{N_o} \end{pmatrix} \qquad (6)$$

Here, reference is made to cell bodies and flagella via the subscripts $q$ and $q + 1$ respectively, where $q = 1, 3, 5, \ldots, 2N_o - 1$. Hence, $\mathbf{U}_q$ and $\boldsymbol{\Omega}_q$ are the respective instantaneous linear and angular velocities of a given cell body, and similar definitions follow for the flagellar velocities $\mathbf{U}_{q+1}$ and $\boldsymbol{\Omega}_{q+1}$. Each element in the above matrix is itself a $3 \times 3$ matrix (where the superscript $T$ denotes the usual matrix transpose operation), because the forces and velocities etc. are three-dimensional vectors and are defined as follows:

- $K_{ijkl}$ is the force in the $i$ direction on the particle $k$ due to the linear translation (with a unit velocity) of particle $l$ in the $j$ direction.
- $L^T_{ijkl}$ is the force in the $i$ direction on the particle $k$ due to the angular rotation (with a unit angular velocity) of particle $l$ in the $j$ direction.
- $L_{ijkl}$ is the torque in the $i$ direction on the particle $k$ due to the linear translation (with a unit velocity) of particle $l$ in the $j$ direction.
- $M_{ijkl}$ is the torque in the $i$ direction on the particle $k$ due to the angular rotation (with a unit angular velocity) of particle $l$ in the $j$ direction.

The indices $i$ and $j$ are cycled through the usual $X$, $Y$, $Z$ directions (which define a fixed set of axes, i.e., they neither rotate nor translate with the organism), while $k$ and $l$ are

assigned values of 1, 2, 3, . . . , $2N_o$. This approach was adopted by Tullock et al. (58) to model the sedimentation of particles inside containers, with particular application to falling ball rheometry.

For each organism, the flagellum rotates relative to the cell body with an angular velocity $\boldsymbol{\omega}_{q+1}$. This rotation takes place about the flagellar axis, the direction of which depends on the organism's orientation. For all organisms, however, the magnitude of the angular velocity $\omega$ is assigned a value of 1 (for all of the present calculations). This, together with the fact that each organism translates as a rigid body, gives rise to the kinematic constraints

$$\mathbf{U}_q = \mathbf{U}_{q+1} \quad \text{and} \quad \boldsymbol{\Omega}_q = \boldsymbol{\Omega}_{q+1} - \boldsymbol{\omega}_{q+1}. \tag{7}$$

Equilibrium requires that for each pair of surfaces, namely, a cell body and flagellum combination, the force and torque must be equal and opposite

$$\mathbf{F}_q = -\mathbf{F}_{q+1} \quad \text{and} \quad \mathbf{T}_q = -\mathbf{T}_{q+1} \tag{8}$$

These furnish the remaining $2N_o$ of the necessary $8N_o$ vector equations ((6)-(8)) for which the $8N_o$ vectors $\mathbf{F}_q$, $\mathbf{T}_q$, $\mathbf{F}_{q+1}$, $\mathbf{T}_{q+1}$, $\mathbf{U}_q$, $\boldsymbol{\Omega}_q$, $\mathbf{U}_{q+1}$, and $\boldsymbol{\Omega}_{q+1}$ may be solved. Of particular interest here are the instantaneous linear velocity $\mathbf{U} = \mathbf{U}_q$ and instantaneous angular velocity $\boldsymbol{\Omega} = \boldsymbol{\Omega}_q$ of each organism. It is worth noting that this procedure (which has been applied, for the special case of a single organism swimming in an unbounded fluid, by Ramia and Tullock (59)) is computationally more efficient than that used by Phan-Thien et al. (34) (and later by Ramia (37)). Briefly, they begin with the discretized boundary integral system equation $\mathbf{Hu} = \mathbf{Gt}$ where $\mathbf{H}$ and $\mathbf{G}$ are the known system matrices. Then, by inversion of $\mathbf{G}$, the boundary traction $\mathbf{t}$ is expressed in terms of the boundary velocity $\mathbf{u}$ which in turn is a function of $\mathbf{U}$ and $\boldsymbol{\Omega}$ (the instantaneous rigid body velocities). Appropriate integration of the traction over the surface of the organism in question yields, from equilibrium considerations, the velocities $\mathbf{U}$ and $\boldsymbol{\Omega}$. With the present approach, however, to assemble all the of elements of the matrix in Eq. 6, solution of the system equation by Gaussian elimination (and not a complete inversion) need be carried out only once, since both $\mathbf{G}$ and $\mathbf{H}$ depend only on the geometry and not on the boundary conditions. Depending on the size of the problem, this could typically represent half the computing time that would be necessary for a complete inversion. Given that there are typically 500 unknowns/organism involved in the system equation, inversion of the $[12N_o, 12N_o]$ resistance matrix in Eq. 6 is by comparison an insignificantly minor task.

## Approximate kinematics scheme

The assumptions and procedures outlined in this section apply to the results of Approximate Kinematic Scheme Results, below (and its subsections, The Swimming of Two Neighboring Organisms, Swimming Near a Half-Space, and Swimming between Two Parallel Plates), which are depicted in Figs. 11, 12, and 13.

The trajectory of any point on the organism's surface is given in terms of two time-dependent transformations, a translation vector and a rotation matrix. The latter is expressed as a function of the three Euler angles, which in turn are determined by the organism's linear and angular velocities at any instant. This procedure is discussed by Keller and Rubinow (60) and has since been applied by Ramia (37); hence only a brief outline is presented here.

Let $\mathbf{r}(t)$ represent any position vector in the cell body fixed $(x, y, z)$ frame (i.e. a frame fixed with respect to the cell body that hereafter will be referred to as the body frame) and $\mathbf{R}(t)$ be this vector referred to the globally fixed $(X, Y, Z)$ frame (see Fig. 6) at a given time $t$. The transformation from $\mathbf{r}(t)$ to $\mathbf{R}(t)$ consists of a translation by $\mathbf{R}_C(t)$ and a rotation by $\mathbf{A}^{-1}(t)$ (Keller and Rubinow (60)):

$$\mathbf{R}(t) = \mathbf{R}_C(t) + \mathbf{A}^{-1}(t)\mathbf{r}(t), \qquad \frac{d\mathbf{R}_C(t)}{dt} = \mathbf{A}^{-1}(t)\mathbf{U}_q(t) \tag{9}$$

where $\mathbf{U}(t) = \mathbf{U}_q$ is the linear velocity of the body frame (i.e., the previously defined instantaneous swimming velocity) and $\mathbf{A}^{-1}(t)$ is a $3 \times 3$ rotation matrix expressible in terms of the Euler angles $\psi_1(t)$, $\psi_2(t)$, and $\psi_3(t)$ (Eq. 4-47 in Goldstein (61)). These angles in turn depend on the angular velocity of the body frame $\boldsymbol{\Omega}_q$ according to the differential equations (Eq. 4-103 in Goldstein (61)):

$$\boldsymbol{\Omega}_q = (\dot{\psi}_2 \sin\psi_1 \sin\psi_3 + \dot{\psi}_1 \cos\psi_3,$$
$$\dot{\psi}_2 \sin\psi_1 \cos\psi_3 - \dot{\psi}_1 \sin\psi_3, \quad \dot{\psi}_2 \cos\psi_1 + \dot{\psi}_3). \tag{10}$$

where the dot notation is used to represent time derivatives. Numerical solution of these equations (with appropriate initial conditions) for the Euler angles specifies the rotation matrix $\mathbf{A}^{-1}$, giving the trajectory of the cell body/flagellar joining point (i.e., the origin) and any point in the body frame $\mathbf{R}_f$ from Eqs. (9). Points on the flagellum rotate with an angular velocity $\boldsymbol{\omega}_{q+1}$ relative to the body frame and may easily be referred to it. The coordinates of such points can in turn be referred to the fixed frame via the first of Eqs. (9), giving the trajectory of any point on the flagellar surface.

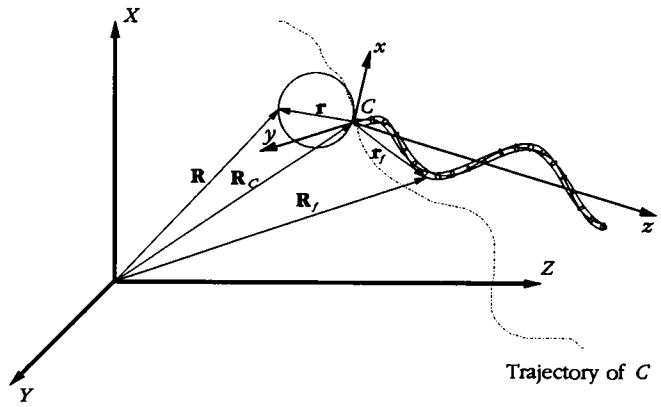


FIGURE 6 Definition of the variables and axes associated with the modeling of swimming kinematics.

As outlined in the flowchart of Fig. 7, a given organism's flagellar phase angle $\theta$ as well as its position $s_d$ and orientation $\phi$ relative to a given boundary (as defined in Fig. 12 *a*) are initially fixed. The BEM is used to calculate the instantaneous velocities $\mathbf{U}$ and $\mathbf{\Omega}$. Next, the flagellar phase angle is incremented (in the same sense as the fundamental flagellar rotation) giving a new flagellar orientation, relative to the supposedly fixed cell body, and again the BEM is used to solve the Stokes problem for the updated geometry and boundary conditions. In this manner, the entire flagellar cycle is scanned and $\mathbf{U}$ and $\mathbf{\Omega}$ may then be expressed as discrete functions of $\theta$ (where $\theta = \omega t$ and $\omega = 1$ throughout). A least-squares regression transforms these into continuous functions of $\theta$. Reference of these functions to the globally fixed $(X, Y, Z)$ frame and substitution into Eqs. (9) and (10) yields the trajectory of any point on the organism. The direction cosines of a given flagellar axis are averaged over the time interval considered (here $16\pi$, which represents 8 flagellar cycles). These averages represent the direction cosines of the axis of propagation. An axial velocity is defined as the ratio of the displacement along the axis of propagation to the elapsed time. It is found that in all of the cases considered, this velocity varies periodically with every flagellar cycle. The mean of this axial velocity, over the time interval considered, which is significantly larger than and an exact multiple of the flagellar period $2\pi$, defines the mean swimming speed $\bar{U}$ for the given position and orientation of the organism.

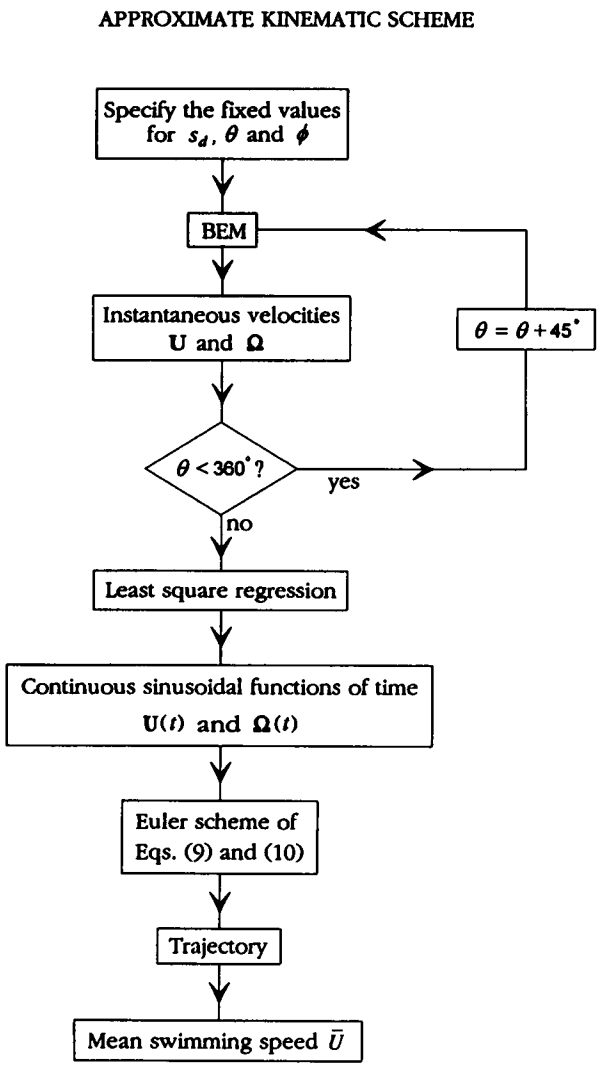


FIGURE 7 Flowchart outlining the steps involved in the approximate kinematic scheme.

Ramia (37) employed the present approximate kinematic scheme to model the swimming of the organism *S. volutans* in an unbounded fluid. Having calculated the swimming velocities for 8 instants/flagellar cycle, it was found that both $\mathbf{U}$ and $\mathbf{\Omega}$ may be approximated (to within 0.5%) by sinusoidal functions of $\theta$, for all perturbations of geometry considered. Similarly, in the present study of the effects of hydrodynamic interactions (i.e., due to boundaries or neighboring organisms) both $\mathbf{U}$ and $\mathbf{\Omega}$ remain sinusoidal functions of $\theta$. Furthermore, calculations for 8 instants/flagellar cycle lead to sufficiently accurate continuous functions of these velocities (again typically less than 0.5% errors are involved). Hence, the sinusoidal function approximation based on results for 8 instants/flagellar cycle, as employed by Ramia (37), is also adopted here.

It is noteworthy that when swimming in an unbounded fluid is being modeled, this "approximate" kinematic approach is actually exact (with respect to the approximate sinusoidal functions). This is the case because, to an observer at rest with respect to the flagellum, only the flagellar phase angle (relative to the cell body) and not the organism's position or orientation is distinguishable. When swimming near boundaries is being modeled, however, both the organism's position and orientation relative to any given boundary become distinguishable to such an observer. Hence, the assumption of fixed organism position and orientation introduces some minor errors. Typical estimates of these errors (as considered under Swimming at 45° toward a Half-Space, below), which consist of a direct comparison of this approximate kinematic scheme with an exact tracking scheme, show that they are not very serious. This is particularly true far away from a given boundary when the separation distance is much greater than the maximum deviation of the joining point trajectory from the axis of propagation.

## Organism tracking scheme

The assumptions and procedures outlined in this section are applicable to the section headed Organism Tracking Results and its subsections, Swimming at 45° toward a Half-Space and Swimming Close and Parallel to a Half-Space.

As outlined in the flowchart of Fig. 8, the flagellar phase angle $\theta$, organism position $s$, and orientation $\phi$ relative to a given boundary are initially specified. Next, the instantaneous swimming linear velocity $\mathbf{U}$ and angular velocity $\mathbf{\Omega}$ are calculated using the BEM. Assuming these velocities to be constant throughout the small but finite time increment $\Delta t$, the position and orientation of the organism are then trans-

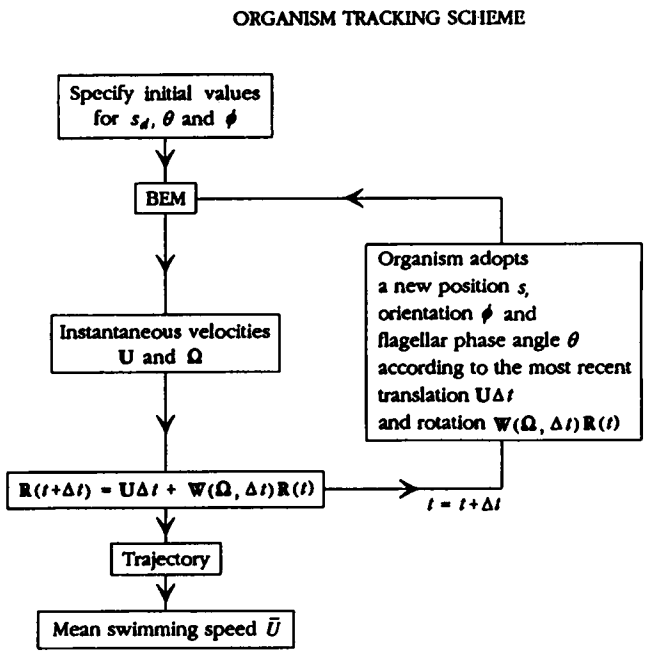


FIGURE 8 Flowchart outlining the steps involved in the organism tracking scheme.

formed according to the equation

$$\mathbf{R}(t + \Delta t) = \mathbf{U}\Delta t + \mathbf{W}(\Omega, \Delta t)\mathbf{R}(t) \qquad (11)$$

where $\mathbf{R}$ is the position vector of any given point on the cell body (as defined in Fig. 6); a similar equation exists for transforming any point $\mathbf{R}_f$ on the flagellum. This transformation is composed of a translation $\mathbf{U}\Delta t$ and a rotation $\mathbf{W}(\Omega, \Delta t)\mathbf{R}(t)$. Here, $\mathbf{W}(\Omega, \Delta t)$ is a matrix representing a rotation through an angle $\Omega\Delta t$ about an axis the direction of which is defined by the direction cosines of the angular velocity vector $(\Omega_x, \Omega_y, \Omega_z)/\Omega$ and which passes through the cell body/flagellar joining point $\mathbf{R}_C$ (Eq. 1.70 of Paul (62)). At the end of each time increment, the newly updated organism discretization defined by $\mathbf{R}(t + \Delta t)$ and $\mathbf{R}_f(t + \Delta t)$ has assumed a new position, and the flagellar phase angle and orientation, along with the appropriate boundary conditions, are then used as new input for the BEM. This cycle is carried out repeatedly for the duration of the given period of interest. The trajectory of any point on either the cell body or the flagellum is given directly by $\mathbf{R}(t)$ or $\mathbf{R}_f(t)$, respectively. In cases where the organism swims without changing its direction of propagation, the mean swimming speed $\bar{U}$ (over the time interval in question) may simply be given as the ratio of the overall distance along the axis of propagation to the elapsed time. On the other hand, when the swimming direction is not constant, it is sufficient to refer to an instantaneous swimming speed which is given by the dot product of $\mathbf{U}$ and the unit vector along the absolute flagellar angular velocity (Keller and Rubinow (60)).

## Mean velocities, forces, and torques

The steps for determining the mean swimming speed $\bar{U}$ depend on whether the approximate kinematic scheme or the organism tracking scheme is employed as well as whether the organism is maintaining a constant swimming direction. This is addressed in sections headed Approximate Kinematics Scheme and Organism Tracking Scheme (above).

The mean angular velocity is simply defined as $\bar{\Omega} = (\bar{\Omega}_x^2 + (\bar{\Omega}_y^2 + (\bar{\Omega}_z^2)^{1/2}$ with $\bar{\Omega}_x$, $\bar{\Omega}_y$, and $\bar{\Omega}_z$ representing the means of the respective components for one flagellar cycle.

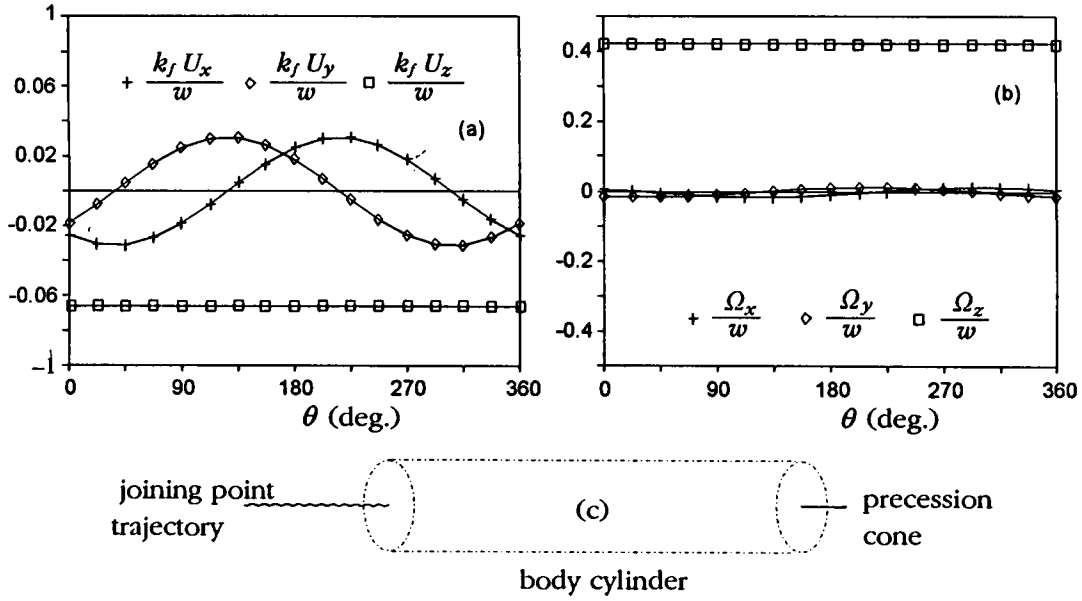


FIGURE 9 Summary of the results for swimming in an unbounded fluid. (*a*) Graphs of the normalized instantaneous swimming velocity components versus the flagellar phase angle $\theta$. (*b*) Graphs of the normalized instantaneous angular velocity components versus the flagellar phase angle $\theta$. (*c*) Summary of the swimming kinematics, showing the trajectory of the cell body/flagellar joining point compared with the *precession cone* and the *body cylinder*.

This definition is sufficient since the radial components $\bar{\Omega}_x$ and $\bar{\Omega}_y$ are both small compared with the axial component $\bar{\Omega}_z$ (see Fig. 9 *b*). Similar definitions are used for the mean propulsive force $\bar{F}$ and the mean propulsive torque $\bar{T}$, since they also have radial, $x$, and $y$ components that are small compared with their axial $z$ component.

## SWIMMING IN AN UNBOUNDED FLUID

Fig. 9 *a* shows the normalized components of linear velocity $k\mathbf{U}/\omega$ as functions of flagellar phase angle $\theta$ for an organism swimming in an unbounded fluid. The axial $z$ component of velocity is constant, and both the $x$ and $y$ radial components are sinusoidal with mean values of approximately zero. Furthermore, these radial components are out of phase with each other in a particular manner such that the magnitude of $\mathbf{U}$ is essentially constant, for any given instant, throughout the flagellar cycle. Fig. 9 *b* shows that the radial components of the normalized angular velocity $\Omega_x$ and $\Omega_y$ vary with a much smaller amplitude than $U_x$ and $U_y$, and both are consistently small compared with their axial component $\Omega_z$.

Fig. 9 *c* shows that the trajectory of the point $C$ describes a helix about the axis of propagation. The amplitude of this helix is small compared to the body cylinder radius (i.e., a cylinder containing the flagellar helical centerline as defined in Fig. 5). Furthermore, the $z$-axis defines a small constant angle with the $Z$-axis and precesses about it with a constant angular velocity depicting (in a frame at rest with respect to the point $C$) a conical surface of revolution (hereafter referred to as the *cone of precession*). Similar findings were reported by Keller and Rubinow (60), who assumed that both radial components of the angular velocity were negligible compared with its axial component and that $\mathbf{U}$ is constant.

Ramia and Tullock (59) determined the mean swimming speed $\bar{U}$ for this organism in three different ways. First, they calculated (using the result of Keller and Rubinow (60)) the dot product of $\mathbf{U}$ and the unit vector along the absolute flagellar angular velocity, from a single instant. Second, they calculated the arithmetic mean of the components of $\mathbf{U}$, i.e., $\bar{U} = (\bar{U}_x^2 + \bar{U}_y^2 + \bar{U}_z^2)^{1/2}$ for the 8 instants/flagellar cycle considered. Third, they considered the trajectory, using the present approximate kinematic scheme, for eight flagellar cycles. The results from all three were basically identical. The resulting mean swimming speed in an unbounded fluid $\bar{U}_\infty$, together with the mean angular velocity $\bar{\Omega}_\infty$, mean propulsive force $\bar{F}_\infty$, and mean propulsive torque $\bar{T}_\infty$ (which as described under Mean Velocities, Forces, and Torques, above, were determined to be arithmetic means of the respective instantaneous results), will hereafter be used as normalizing factors.

Many of the above-mentioned early pioneering models (see, for example, Gray and Hancock (26) and Chwang and Wu (28)) neglect the most fundamental hydrodynamic interaction, namely, the interaction between the cell body and the flagellum. Their approach to locomotion was a rather simplistic one. Basically, a rotating helical flagellum induces a propulsive force and torque on the inert cell body (typically presumed to be spherical), and the entire organism acquires an instantaneous swimming velocity $\mathbf{U}$ and a counter-rotational angular velocity $\mathbf{\Omega}$, thereby conserving linear and angular momentum. Hence, the flagellum produces the necessary propulsion and the cell body dissipates it in the form of drag. This section is concerned with estimating the typical errors involved in this kind of approach.

Consider a flagellum rotating in isolation (i.e., in an unbounded fluid and not attached to a cell body), thereby producing a propulsive force $F_i$ (here the magnitude of the mean force is the same as that of the instantaneous force). Then the difference $\Delta F = F - F_i$ between this and the actual propulsive force $F$, with the cell body present (still in an otherwise unbounded fluid), represents the effect of the cell body/flagellar hydrodynamic interaction on the flagellar propulsive force. The flagellar contribution to translational drag $D_T$ is the difference between the actual drag on the organism and the drag on the spherical cell body alone. Similar definitions follow for the effect of hydrodynamic interaction on the flagellar propulsive torque $\Delta T = T - T_i$ and for the flagellar contribution to rotational drag $D_R$.

Fig. 10 *a* shows (in normalized form) the effect of the cell body/flagellar hydrodynamic interaction on the flagellar propulsive force $\Delta F/F$ and torque $\Delta T/T$, along with the flagellar contribution to translational drag $D_T/F$ and rotational drag $D_R/T$ as functions of the normalized flagellar wave number $\alpha_f k_f$. As $\alpha_f k_f$ increases, $\Delta F/F$ and $\Delta T/T$ both increase, while $D_T/F$ and $D_R/T$ decrease, with the trends being more prominent for the force and translational drag. The increase in propulsive force and torque is probably due to a progressively larger proportion of the flagellum being in closer proximity of the cell body, as the wave number increases (compare Fig. 10 *b* and *c*). For realistic flagellar geometries (i.e., $\alpha_f k_f \approx 1$), $\Delta F/F$ is approximately equal to $D_T/F$. But, as $\alpha_f k_f$ increases beyond such realistic values, the effect of the cell body/flagellar hydrodynamic interaction on the propulsive force greatly overshadows the flagellar contribution to drag. On the other hand, $\Delta T/T$ is much smaller than $D_R/T$, for all values of $\alpha_f k_f$.

Fig. 10 *d* shows results like those presented in Fig. 10 *a*, except that they relate to variations in the number of flagellar wavelengths $N_{\lambda_f}$. As $N_{\lambda_f}$ increases, both translational and rotational flagellar contributions to drag increase, with the increase being much steeper for the rotational case. For $N_{\lambda_f} = 0.5$, the case depicted in Fig. 10 *e*, the flagellum is very asymmetric and has a large amplitude, resulting in a propulsive force and torque with significantly large radial components. This may be the cause for the irregular spike in $\Delta F/F$ and $\Delta T/T$ for $N_{\lambda_f} < 1$. For all other, more realistic values of the number of wavelengths (i.e., $N_{\lambda_f} \geq 1$), $\Delta F/F$ is approximately equal to $D_T/T$, and $\Delta T/T$ is much smaller than $D_R/T$.

The results of Fig. 10 show that the simplistic approach of early models would perform well in terms of swimming velocity predictions and for realistic flagellar geometries and poorly in terms of angular velocity predictions under any

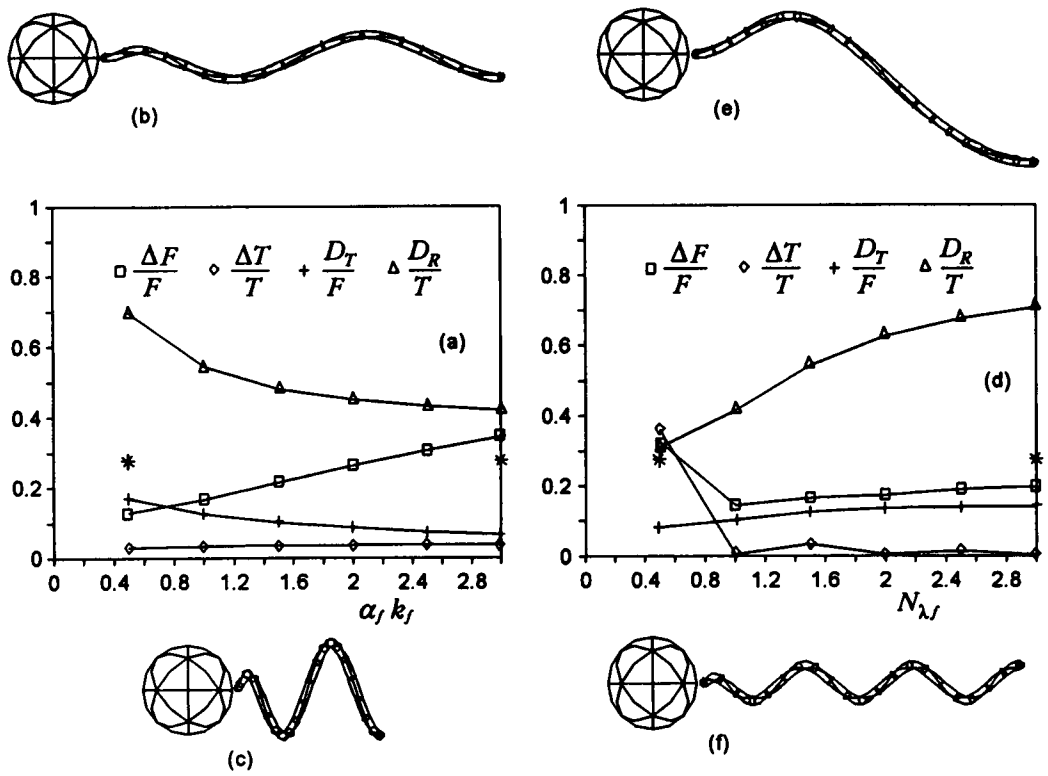


FIGURE 10 Summary of the effects of cell body/flagellar hydrodynamic interaction. (*a*) Graphs of the normalized change in the flagellar propulsive force $\Delta\bar{F}/\bar{F}$ and torque $\Delta\bar{T}/\bar{T}$, and normalized flagellar contribution to translational drag $D_T/F$ and rotational drag $D_R/T$ versus the dimensionless flagellar wave number $\alpha_f k_f$. (*b*) Geometry of the organism on the lower end of the scale, with $\alpha_f k_f = 0.5$ (denoted by a * in (*a*)). (*c*) Geometry of the organism on the higher end of the scale, with $\alpha_f k_f = 3.0$ (denoted by a * in (*a*)). (*d*) As for (*a*), except that the quantities are plotted as functions of the number of flagellar wavelengths $N_{\lambda_f}$. (*e*) As for (*b*), with $N_{\lambda_f} = 0.5$. (*f*) As for (*c*), with $N_{\lambda_f} = 3.0$.

circumstances. Hence, this approach may be useful for modeling the locomotion of organisms with realistic geometries, but its application to an optimization study would surely have major limitations. An example of this is the RFT model of Chwang and Wu (28), which neglects both the cell body/flagellar hydrodynamic interaction and the flagellar contribution to drag. Certainly, there are significant discrepancies between the predicted optimal dimensions and proportions of this RFT model and those predicted by the SBT model of Higdon (21) (which was later shown to agree very closely with the BEM model of Phan-Thien et al. (34)).

## APPROXIMATE KINEMATIC SCHEME RESULTS

The normalized minimum separation distance referred to in the graphs of Figs. 11–14 is defined as follows:

$$s = \frac{s_d - a_f}{\alpha_f} \tag{12}$$

where $s_d$ is the minimum separation distance as defined in Figs. 11 *a*, 12 *a*, and 13 *a*, the flagellar radius $a_f$ is maintained constant at $\approx$1.31, and $\alpha_f = 1$ is used (both here and elsewhere in the present study) as a normalizing factor. Hence, for $s = 0$, the smallest value considered, no part of the organism surface is closer to the half-space than one flagellar radius.

## The swimming of two neighboring organisms

Taylor (12) postulated that two neighboring organisms swimming (by executing planar sinusoidal flagellar waves) may derive a propulsive advantage by beating their flagella in unison (i.e., with constant relative flagellar phase angle and the same frequency). Although this prediction was based on a simplified two-dimensional model, it was consistent with the frequent experimental observation that the flagella of neighboring spermatozoa have a tendency to beat in this manner. No similar model has yet been proposed regarding the case of propulsion by helical flagellar rotation.

Fig. 11 *a* shows that in modeling the swimming of two organisms that are close and parallel to each other, there are two parameters involved: the relative flagellar phase angle $\Delta\theta$ and the minimum separation distance $s_d$. Fig. 11 *b* shows the components of normalized linear velocity $k_f U/\omega$, for each of the two organisms, as functions of the flagellar phase angle (The graph of angular velocity components versus $\theta$ is not included here because it differs negligibly from that for an unbounded fluid), for $\Delta\theta = 0$ and $s = 0$ (i.e., $s_d = a_f$ as defined in Eq. 12). The axial $Z$ components of velocity are nearly the same for the two organisms, as are the $X$ components. Although both $Y$ components of velocity appear to be sinusoidal with the same amplitude and phase angle, they have means (over a flagellar cycle) that are approximately equal in numerical value but opposite in sense. This implies

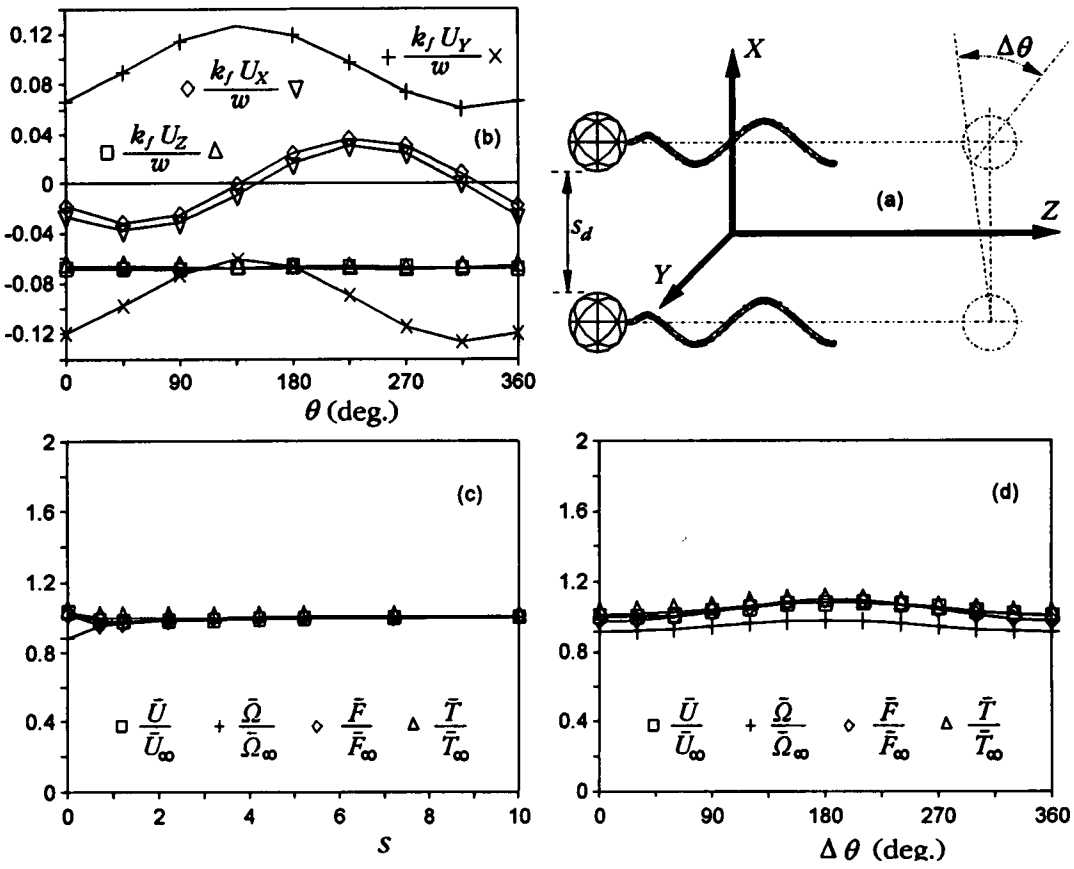


FIGURE 11 Summary of the results for two organisms swimming near and parallel to each other. (*a*) definition of the minimum separation distance $s_d$ and the relative flagellar phase angle $\Delta\theta$. (*b*) Graphs of the normalized instantaneous swimming velocity components for each of the two organisms versus the flagellar phase angle $\theta$. (*c*) Graphs of the normalized mean swimming speed $\bar{U}/\bar{U}_\infty$, mean angular velocity $\bar{\Omega}/\bar{\Omega}_\infty$, mean flagellar propulsive force $\bar{F}/\bar{F}_\infty$, and mean flagellar propulsive torque $\bar{T}/\bar{T}_\infty$ versus the minimum separation distance $s$ (for $\Delta\theta = 0$). (*d*) As for (*c*), except that the quantities considered are plotted as functions of the relative flagellar phase angle $\Delta\theta$ (for $s = 0.5$).

that, should two such organisms be constrained to swim in this close proximity and with a zero relative flagellar phase angle, they would tend to swim out of the plane that initially contains their parallel flagellar axes (each to a different side of this plane at ≈60°). This serves to further reinforce the conjecture of Taylor (12) that where possible neighboring microorganisms are more likely to execute planar flagellar waves (in unison) as opposed to three-dimensional helical rotation. Although this would render the present modeled situation unrealistic, its consideration does yield valuable results regarding the effects of interorganism hydrodynamic interaction on flagellar propulsive forces and torques.

Fig. 11 *c* shows the normalized mean swimming speed $\bar{U}/\bar{U}_\infty$, angular velocity $\bar{\Omega}/\bar{\Omega}_\infty$, propulsive force $\bar{F}/\bar{F}_\infty$, and propulsive torque $\bar{T}/\bar{T}_\infty$ as functions of the normalized minimum separation distance $s$, for $\Delta\theta = 0$. Unless the two organisms are extremely close (with $s < 1$), the results for all four quantities are essentially the same as for the case of an unbounded fluid. This is not surprising when compared with the results of Fig. 10, which show that (for the typical organism defined under Geometrical Modeling, above), in an unbounded fluid, the cell body/flagellar hydrodynamic interaction alters the propulsive force by ≈20% and the propulsive torque by less than 5%. It is expected that interorganism hydrodynamic interaction would never be as significant (regardless of how small the separation distance is) as the more fundamental cell body/flagellar interaction. This, together with the fact that the resistance coefficients for each of two translating or rotating neighboring spheres do not increase significantly (see Happel and Brenner (33)), is the reason for the somewhat uneventful results of this figure.

Fig. 11 *d* shows results like those in Fig. 11 *c*, except that they relate to variations in the relative flagellar phase angle $\Delta\theta$, for $s = 0.5$. Again, the differences between these results and those for an unbounded fluid are not very significant, since they do not exceed 10%. But a slight hydrodynamic coordination is apparent at $\Delta\theta = 180°$, where both the propulsive force and torque and, consequently, swimming speed and angular velocity are at their maximum value. Here, the two organisms are subjected to somewhat unrealistic constraints, namely, their need to remain parallel and close to each other as well as to rotate with the same flagellar angular frequency. Hence the existence of an optimal relative flagellar phase angle could bear some significance, whereas its numerical value and the value of the resulting swimming speed may not. A complete model would necessarily involve a more comprehensive tracking scheme (such as that described under Organism Tracking Scheme, above) allowing

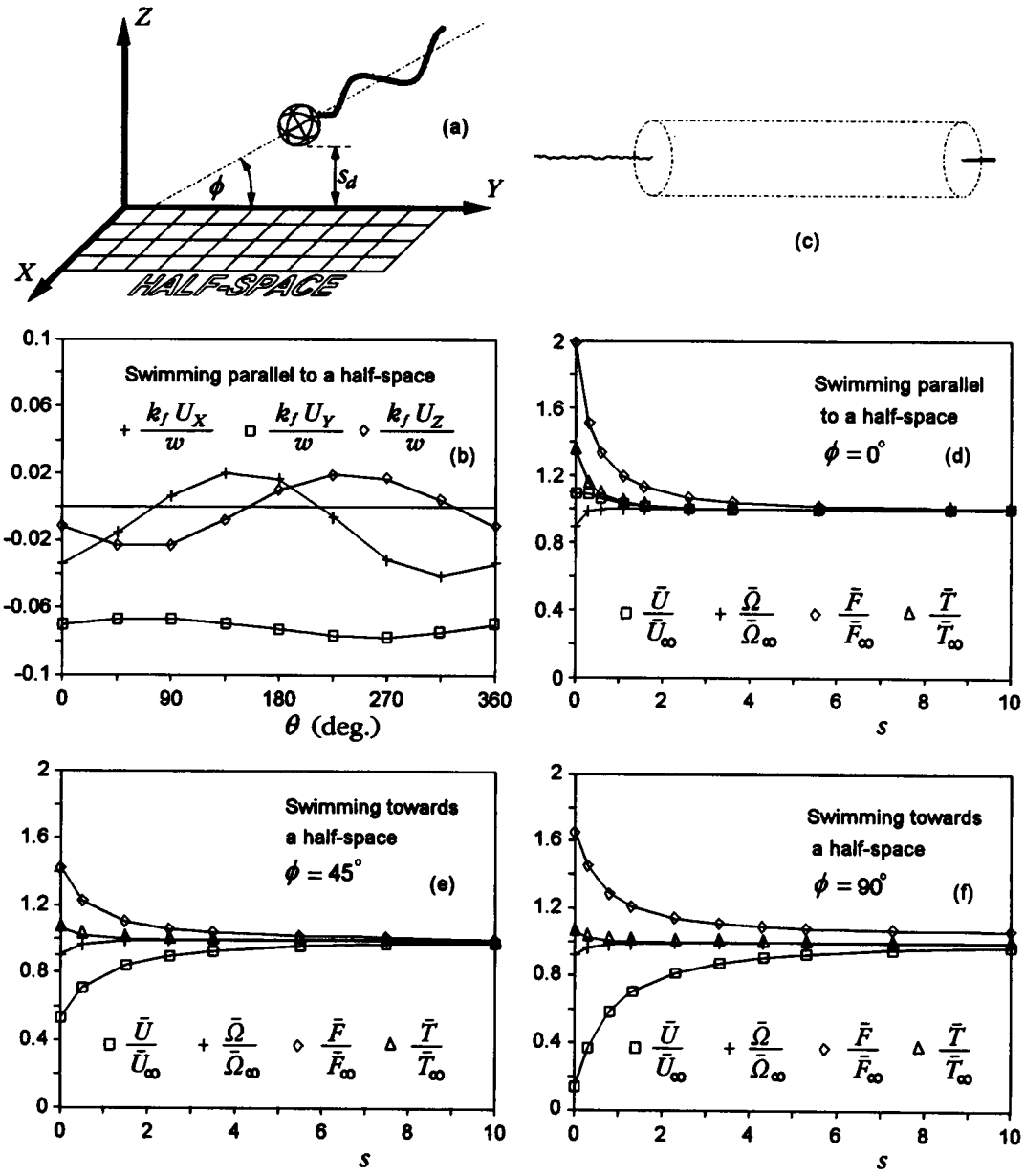


FIGURE 12 Summary of the results for swimming near a half-space. (*a*) Definition of the minimum separation distance $s_d$ and the orientation angle of the flagellar axis $\phi$ relative to the half-space. (*b*) Graphs of the normalized instantaneous swimming velocity components versus the flagellar phase angle $\theta$, for $\phi = s = 0$. (*c*) Summary of the swimming kinematics, for the case of swimming very close and parallel to a half-space (again, $\phi = s = 0$). (*d*) Swimming parallel to a half-space ($\phi = 0$); graphs of the normalized mean swimming speed $\bar{U}/\bar{U}_\infty$, mean angular velocity $\bar{\Omega}/\bar{\Omega}_\infty$, mean flagellar propulsive force $\bar{F}/\bar{F}_\infty$, and mean flagellar propulsive torque $\bar{T}/\bar{T}_\infty$ versus the minimum separation distance $s$. (*e*) Swimming toward a half-space at an angle of 45° (i.e., $\phi = 45.0°$); graphs as in (*d*). (*f*) Swimming normal to and toward a half-space (i.e., $\phi = 90.0°$); graphs as in (*d*).

for the simultaneous variation of $s$, the relative organism orientations, and each of the (not necessarily equal) flagellar rotation frequencies $\omega$. However, for a two-organism problem, this would be very expensive computationally (perhaps an appropriate subject for a future study), but without such a treatment, no further conclusions may be made regarding swimming kinematics or efficiency.

## Swimming near a half-space

Fig. 12 *a* shows the definition of the two parameters involved in modeling the swimming of a microorganism near a half-space. These are the minimum separation distance from the half-space $s_d$ (or in normalized form $s$ as given by Eq. 12) and the angle between the flagellar axis and the half-space $\phi$. Fig. 12*b* shows the components of linear velocity as functions of the flagellar phase angle, for an organism swimming very close (with $s = 0$) and parallel to a half-space. Here (as in The Swimming of Two Neighboring Organisms, above) the corresponding graph for angular velocity closely resembles that for an unbounded fluid (see Fig. 9 *b*) and has not been included. Again, the variation of each of these components is sinusoidal, but unlike the case of an unbounded fluid depicted in Fig. 9 *a*, the axial component (here, the axial

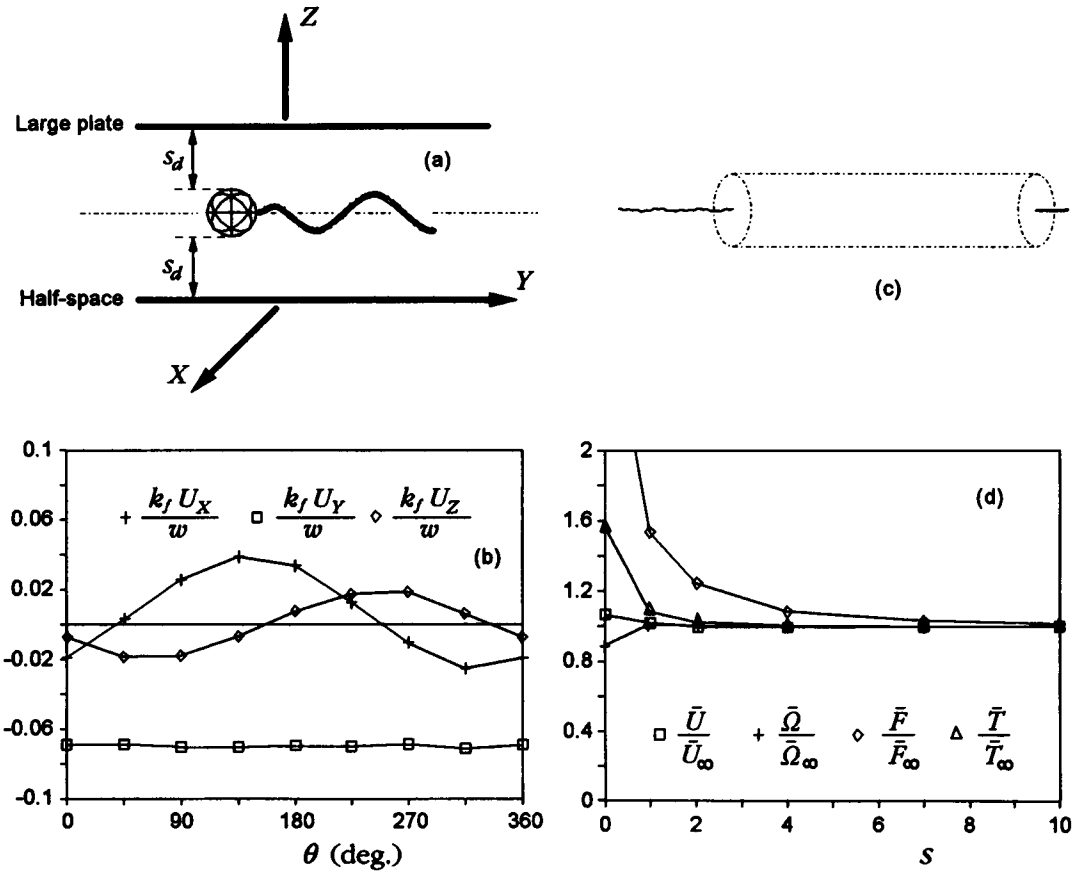


FIGURE 13 Summary of the results for swimming parallel to and midway between two parallel plates. (*a*) Definition of the minimum separation distance from either plate $s_d$. (*b*) Graphs of the normalized instantaneous swimming velocity components versus the flagellar phase angle $\theta$, again for $s = 0$. (*c*) Summary of the swimming kinematics for the case of very small plate separation (i.e., $s = 0$). (*d*) Graphs of the normalized mean swimming speed $\bar{U}/\bar{U}_\infty$, mean angular velocity $\bar{\Omega}/\bar{\Omega}_\infty$, mean flagellar propulsive force $\bar{F}/\bar{F}_\infty$, and mean flagellar propulsive torque $\bar{T}/\bar{T}_\infty$ versus the minimum separation distance $s$.

$z$ component coincides with the $Y$ direction because $Z = 0$ defines the half-space) has a notable amplitude. Although it is not clearly visible in Fig. 12 *c*, the trajectory appears to have lost the helical symmetry, which is characteristic of the case of the unbounded fluid, while maintaining a small but variable amplitude. The angle of precession maintains a small but varying value. Such effects on the swimming kinematics are surprisingly minor and may easily be attributed to the asymmetry introduced by the presence of the half-space.

Fig. 12 *d* shows the normalized mean swimming speed $\bar{U}/\bar{U}_\infty$, angular velocity $\bar{\Omega}/\bar{\Omega}_\infty$, propulsive force $\bar{F}/\bar{F}_\infty$, and propulsive torque $\bar{T}/\bar{T}_\infty$ as functions of the normalized minimum separation distance $s$, for $\phi = 0$. For this case of swimming parallel to the half-space, all parts of the flagellum are, in an approximate average (with respect to time) sense, equally distant from the half-space. Hence, propulsive forces and torques result which are greater, for the given separation distances, than those resulting from any other organism orientation considered in this section. Katz and Blake (30) proposed that the flagellar propulsive force is directly proportional to the ratio of normal to tangential resistance coefficients $\gamma_1 = C_n/C_t$ and the ratio of bi-normal to tangential resistance coefficients $\gamma_2 = C_b/C_t$. Furthermore, the power dissipated by the flagellum increases independently with each of the resistance coefficients $C_t$, $C_n$, and $C_b$. These propositions are consistent with the observation that the general trends (of slow followed by sharp increases, as the distance from the half-space diminishes) for $\bar{F}$ and $\bar{T}$ (in Fig. 12 *d*) resemble those for $\gamma_2$ and $C_t$ (in Fig. 4 *c*), respectively. Here, the torque $\bar{T}/\bar{T}_\infty$ is representative of the power dissipation $\bar{T}\omega$ that is needed to maintain flagellar rotation with the presumed constant angular frequency $\omega$ relative to the cell body.

Fig. 3 *c* shows that a sphere translating in a direction parallel to a half-space or rotating about an axis that is parallel to this half-space will experience progressively more resistance to motion as its distance from this half-space decreases. Despite the apparent flagellar propulsive advantages, such increases in translational and rotational drag on the spherical cell body hinder any significant increase in $\bar{U}$ and cause a decrease in $\bar{\Omega}$, for swimming parallel to a half-space. It is likely that each organism would have a maximum power that it could expend. This may, in turn, limit

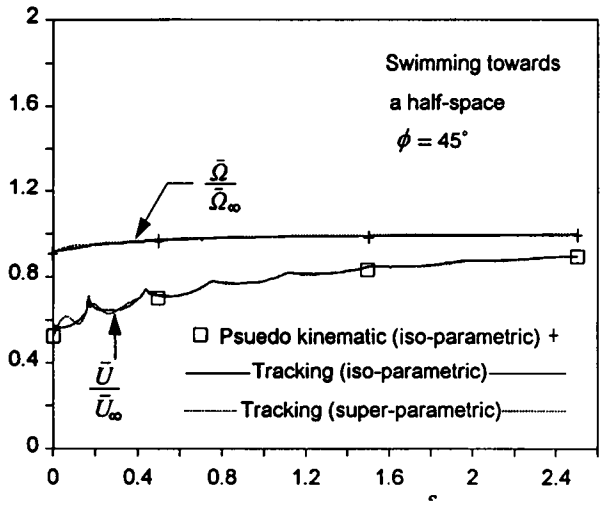


FIGURE 14 Results for swimming toward a half-space at an angle of 45.0° ($\phi$ = 45.0°): graphs of the normalized mean swimming speed $\bar{U}/\bar{U}_\infty$ and mean angular velocity $\bar{\Omega}/\bar{\Omega}_\infty$ versus the minimum separation distance $s$ (results due to the tracking scheme using either isoparametric or superparametric elements are also included).

its flagellar angular frequency, which would consequently lead to a reduction in both $\bar{U}$ and $\bar{\Omega}$. Given this, together with the fact that $\bar{U}$, $\bar{\Omega}$, $\bar{F}$, and $\bar{T}$ are each proportional to $\omega$ (due to the presumed linearity of the fluid), $\omega$ is commonly used as a normalizing factor and treated as an independent parameter.

Fig. 12 *f* shows results similar to those of Fig. 12 *d*, except that they relate to an organism swimming normal to and toward a half-space. Here, the increases in propulsive force and torque are generally less significant than those of the parallel case (in Fig. 12 *d*). This is to be expected because, in an average sense, the flagellum is situated further away from the half-space than in the parallel case, for a given value of $s$. A similar trend for angular velocity results, but a very sharp drop in $\bar{U}$ is predicted, despite the sharp increase in $F$. The rationalization for these trends lies in the results of Fig. 3 (*c* and *d*). There is little difference between the rotational drag on a sphere rotating about an axis that is parallel and one that is normal to the half-space. But for a sphere translating at a distance of ($h/a$) from a half-space the resistive force arising from motion that is parallel to the half-space varies as $\ln(h/a)$, whereas that for normal motion varies as $(h/a)^{-1}$ (Kim and Karrila (41)). In an approximate sense, for the range of separation distances considered here (i.e., $(h/a) \leq 10$), the resistance to normal motion is typically 5 times greater than that for parallel motion (compare Fig. 3, *c* and *d*). Hence, it would appear that in swimming normal to and toward a half-space, the increase in the cell body drag (which is closer to the half-space than the flagellum) grossly outweighs the advantages of a higher flagellar propulsive force.

The results of Fig. 12 *e*, which relate to the case of swimming at 45° to and toward a half-space, bear a qualitative resemblance to those of Fig. 12 (*d* and *f*) and may be explained in a similar manner. Again, the propulsive force increases as the organism swims closer to the wall. However, its maximum value is lower than those of Fig. 12 (*d* and *f*). This may be due to a larger proportion of the flagellum moving in a perpendicular mode (as in Fig. 4 *b*) than for the other two cases ($\phi$ = 0° and $\phi$ = 90°), because for the flagellar geometry employed, the pitch angle is 45°. If this is the case then, the less significant increases in $C_t$ and $\gamma_1$ (compare Fig. 4, *c* and *d*) would be sufficient to explain the resulting trend for $\bar{F}$ (as well as for $\bar{T}$). Here, the resistances to motion of a sphere parallel and perpendicular to the half-space are relevant, with the perpendicular component being more prominent. Hence it is not surprising that the resulting trends for $\bar{U}$ and $\bar{\Omega}$ represent a mediating combination of those exhibited by Fig. 12 (*d* and *f*).

## Swimming between two parallel plates

Experimental observations of the swimming of microorganisms is usually carried out on a fluid solution containing the motile cells, which has been squeezed into a thin film between a microscopic plate and a coverslip. The resulting hydrodynamic effects between a given observed organism and either or both of the plates (as well as other organisms) may affect the measured swimming linear and angular velocities. For this reason, the modeling of an organism swimming midway between and parallel to two large flat parallel plates (see Fig. 13 *a*) considered here is of great interest to experimental observers.

Fig. 13 *b* shows the variation of the linear velocity components as functions of the flagellar phase angle $\theta$, for $s$ = 0. Again, the variations of angular velocity components, with $\theta$, are similar to those for an unbounded fluid and have not been included. Unlike the small but finite amplitude for the axial component (again, this coincides with the $Y$ direction because $Z$ = 0 defines the half-space) exhibited by Fig. 12 *b*, here (Fig. 13 *b*) the amplitude for $U_Y$ appears to have nearly vanished. This may be a consequence of the second wall (i.e., the top plate) negating the asymmetry that the presence of a single wall had introduced. The nearly straight swimming trajectory and the small angle of precession (see Fig. 13 *c*) may also be attributed to this. The radial components $U_X$ and $U_Z$ of velocity with means, over a flagellar cycle, that are much closer to zero than that of the axial component $U_Y$ are a further indication of a kinematically efficient swimming motion. Hence, it generally appears that in swimming between such unrealistically close parallel walls, hydrodynamic interactions have the effect of preventing the organism from colliding with either boundary.

Fig. 13 *d* shows the normalized mean swimming speed $\bar{U}/\bar{U}_\infty$, angular velocity $\bar{\Omega}/\bar{\Omega}_\infty$, propulsive force $\bar{F}/\bar{F}_\infty$, and propulsive torque $\bar{T}/\bar{T}_\infty$ as functions of the normalized minimum separation distance $s$. For this case, the flagellar propulsive advantage is derived from an increase in the resistance coefficients $C_t$, $C_n$, and $C_b$ (Katz and Blake (30)) and ratios of such coefficients $\gamma_1$ and $\gamma_2$ for a slender rod moving midway between two parallel plates (see Fig. 4, *e* and *f*). Generally, the trends exhibited by Fig. 4 (*e* and *f*) regarding

the resistance coefficients for a slender rod moving between two plates are very similar to those of Fig. 4 (*c* and *d*) regarding motion near a half-space. The exceptions are the trends for $\gamma_1$ (with the rod in parallel orientation; Fig. 4 *e*) and for $C_t$ (with the rod in perpendicular orientation; Fig. 4 *f*) showing notably more severe increases than the corresponding trends for motion near a half-space (Fig. 4, *c* and *d*). Hence, noticeably sharper increases result in propulsive force and propulsive torque, compared with swimming parallel to a half-space (considered in Fig. 12 *d*). The equally steep increase in resistance to translation of the spherical cell body between two plates (see Fig. 3 *e*) compensates for the excessive propulsive force, yielding a swimming speed which, by comparison, differs negligibly from that of an organism swimming in an unbounded fluid. A similar explanation may generally follow for the swimming angular velocity. Certainly, for the case of closest approach considered here, the resistance to rotation appears to have overshadowed the excessive propulsive torque, leading to a decrease in $\bar{\Omega}$.

## ORGANISM TRACKING RESULTS

The present tracking scheme was successfully employed by Vincent et al. (63) in a BEM study of trajectories of sedimenting particles. They argued that for infinitesimal time increments this approach would be exact. Furthermore, the inherent error is $O(\Delta t)$, and it may be maintained at an acceptably low value, at the expense of lengthy computations. Its performance is currently assessed via the two examples in the next two sections.

### Swimming at 45° toward a half-space

The case of a single organism swimming at 45° to and toward a half-space is considered. The quantities $\bar{U}/\bar{U}_\infty$ and $\bar{\Omega}/\bar{\Omega}_\infty$ (as calculated using the approximate kinematic scheme) are compared with the normalized instantaneous swimming speed (given by Keller and Rubinow (60); i.e., the dot product of **U** and the unit vector along the absolute flagellar angular velocity) and the normalized instantaneous angular velocity (as calculated at every instant with the tracking scheme), respectively. This is shown in Fig. 14 where results, due to the tracking scheme, from both isoparametric and superparametric elements are also included.

For $s \geq 0.5$ there is negligible difference between the two schemes, as well as between the results due to the different types of elements. For $s < 0.5$, however, good agreement is still apparent for the angular velocity, but minor discrepancies emerge among the three sets of results for the swimming speed. The errors introduced by fixing the organism's position and orientation, in the approximate kinematic scheme, are, expectedly, progressively more apparent as the organism comes very close to the half-space. This is reflected by the periodic variation in swimming speed (predicted by the tracking scheme), which is superimposed on the otherwise generally slowly decaying trend, increasing in amplitude as the organism swims closer to the half-space. Furthermore, the apparent differences between these variations (in this region where $s < 0.5$), as calculated with the two element types, indicate the increasing sensitivity of the instantaneous velocities to the discretization scheme. Finally, it is noteworthy that for the calculations made with the tracking scheme, 40 instants/flagellar cycle were considered. These calculations were then repeated with only 20 instants/flagellar cycle, for the isoparametric elements, and the resulting differences were negligible. Hence, it may safely be concluded that the approximate kinematic scheme does yield realistic predictions of the effects of hydrodynamic interaction on the swimming of microorganisms.

### Swimming close and parallel to a half-space

Fig. 15 shows two orthogonal views of the trajectory for an organism swimming very close (again, the minimum separation distance is $\approx a_f$) and parallel to a half-space as predicted by the present BEM and tracking scheme. On a local scale (i.e., within one flagellar cycle) the trajectory appears to be consistently helical with a small amplitude. Of particular interest is the overall shape of the swimming path in the *X–Y* view, because this corresponds to what might be seen through a microscope during experimental observation when an organism swims very close to the microscopic plate. Here, for the time interval considered, the predicted overall path of swimming appears to be circular, in this view. Furthermore, the radius of the circular path is of a magnitude similar to that of the length of the organism ($\approx 10$ $\mu$m). This is consistent with the experimental observations of Berg and Turner (4), who report that when *E. coli* swims near a planar boundary it tends to swim in spirals rather than straight lines.

The rationalization for the above-mentioned "circular" swimming paths lies in the results of Fig. 12 *b*. This shows the variation of the linear velocity components with the flagellar phase angle for an organism maintained near and

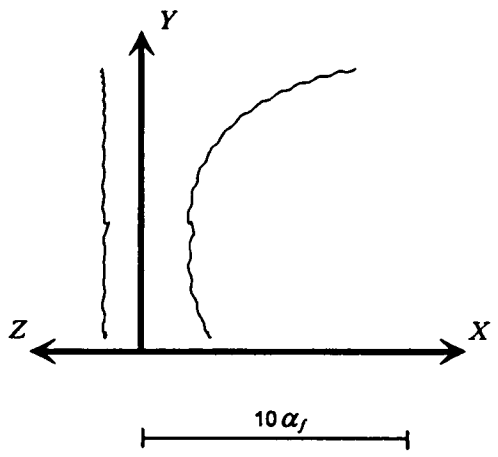


FIGURE 15 Two orthogonal views of the swimming path for an organism swimming very close to and parallel to a half-space (defined by $Z = 0$).

parallel to a half-space. Much like the case of the unbounded fluid, the axial $Y$ velocity component is consistently negative, and the radial $Z$ component, which is normal to the half-space, is negligible when averaged over a full flagellar cycle. The remaining radial $X$ component, however, which is parallel to the half-space, does not average out to zero over a flagellar cycle (which may be attributed to the asymmetry in the propulsive force introduced by the presence of the half-space). This would cause a net sideward displacement of the organism with each flagellar cycle. Due to symmetry this displacement would be of the same magnitude for each and every flagellar cycle. Hence, a circular path would be a logical outcome, but it is not directly deducible from the results of Fig. 12 *b*; hence the application of the organism tracking scheme becomes necessary.

When a microorganism swims below a given boundary rather than above it (such as near a coverslip), Berg and Turner (4) observe that while it maintains the same sense for its flagellar rotation, the sense of its spiral swimming path reverses. This may be explained purely through an argument based on symmetry, namely, that a spiral drawn on a piece of paper could appear clockwise or anticlockwise, depending on whether it is viewed from above or below the paper it is drawn on.

A more detailed quantitative comparison between the experimental observations of Berg and Turner (4) and the present numerical model is currently infeasible. There are several reasons for this. First, unlike the ideal organism modeled here, the observed organism *E. coli* posses a flagellar bundle in which not all filaments share a common basal site. Second, the observations of Berg and Turner (4) relate to a boundary that is not exactly flat but has a radius of curvature (in one plane) of 50 $\mu$m compared with an organism having a typical length of $\approx$10 $\mu$m. Third, it would be difficult to ascertain, from observations with a microscope, whether an organism is maintaining a constant distance from the given boundary. Finally, with regard to numerical modeling, the organism exhibited a slow but steady migration toward the half-space and hence a tendency to crash into it. Prior to crashing, when any given node on the discretized organism may be much closer to the half-space than it is to its nearest vertex, numerical instabilities become prominent. This is particularly evident in Fig. 15 near the part of the swimming path when the organism is swimming downward in the negative $Y$ direction.

## CONCLUSIONS

The effects of the presence of neighboring walls on the resistance coefficients of spheres and slender rods have been modeled using the BEM. Comparison with existing SBT and reflection solutions was generally very good. This method is used to investigate the effect of cell body/flagellar hydrodynamic interaction on the swimming speed and angular velocity of an organism swimming in an unbounded fluid. It is concluded that this effect, which was neglected in early pioneering models, is generally considerably less significant than the flagellar contribution to drag.

This BEM is adapted to account for all hydrodynamic interactions arising when an organism swims in the vicinity of plane boundaries or other organisms. The case of two neighboring organisms swimming close and parallel to each other was considered. It was apparent that, on the whole, hydrodynamic interactions between two such organisms were less significant than those between the cell body and the flagellum of a given single organism. For organisms swimming very close to each other, a minor hydrodynamic coordination (which maximizes both $\bar{F}$ and $\bar{T}$ and consequently $\bar{U}$ and $\bar{\Omega}$) exists.

Modeling the swimming of an organism near and parallel to a single wall or midway between two such walls bears valuable physical significance. This is because, often when such an organism is observed, it is swimming close to and parallel to a microscopic plate or between this plate and a coverslip. Here, it is predicted that, for either of these cases, both the measured swimming speed and angular velocity (if appropriately normalized with respect to the presumed constant fundamental flagellar frequency $\omega$) vary by less than 10% from their corresponding values in an unbounded fluid. This is explained in terms of the flagellar propulsive advantage derived from an increase in the ratio of the normal to tangential resistance coefficients of a slender body being offset by the apparently equally significant increase in the cell body drag. The organism will need to dissipate more power, however, to maintain these swimming speeds and angular velocities. If in reality this power is limited by biophysical constraints, then the organism would be observed to drastically reduce its flagellar rotation frequency, which in turn reduces its swimming speed and angular velocity.

The validity of the approximate kinematic scheme is confirmed via its direct comparison with the organism tracking scheme. It is concluded that when the mean swimming speed and other mean quantities are sought, the approximate kinematic scheme is sufficient. When the swimming path over several flagellar cycles is of interest, the tracking scheme must be utilized. For the case of swimming very close and parallel to a half-space, the tracking scheme predicts a circular swimming path, which is in agreement with the observations of Berg and Turner (4).

In conclusion, it may safely be stated that in all cases modeled here, hydrodynamic interaction is significant only when the relevant separation distances (see Figs. 11*a*, 12*a*, and 13*a*) are approximately equal to or smaller than the largest physical dimension of the organism in question. This is immediately apparent from all results shown in Figs. 11, 12, and 13, where separation distances of up to 11.31 (because $s_d = s + a_f$, $s \leq 10$ and $a_f = 1.31$) were considered in modeling the swimming of an organism the flagellar axial extension of which is $\approx$13 (i.e., as defined in Fig. 5, $z_m \approx 13$). Furthermore, in many of the physically relevant cases, within the small range considered, the hydrodynamic effects remain insignificant. It is also reassuring that the use of materials such as petroleum gels for mounting coverslips onto

microscopic plates is common practice (see, for example, Swan (64)). This tends to prevent fluid drift as well as provide a good depth of fluid (a fluid film thickness of up to two orders of magnitude greater than the largest dimension of the organism is attainable), thereby greatly reducing the likelihood of significant hydrodynamic interactions.

## APPENDIX 1: UNBOUNDED AND HALF-SPACE KERNELS

For an unbounded fluid, Brebbia et al. (43) give the Kelvin solution for the fundamental velocity and traction kernels $u_{ij}^K$ and $t_{ij}^K$, respectively, as

$$u_{ij}^K = \frac{1}{8\pi\mu}\left(\frac{\delta_{ij}}{r} + \frac{r_i r_j}{r^3}\right) \quad \text{and} \quad t_{ij}^K = -3\frac{r_i r_j r_m n_m}{4\pi r^5} \tag{13}$$

where $\mathbf{r} = \mathbf{x} - \mathbf{X}$ (see Fig. 1), $\mathbf{x}$ is the position vector of the field point, and $\mathbf{X}$ is the point where the Stokeslet is situated. Here, $n_j$ is a unit vector pointing out of the flow domain, and $\delta_{ij}$ is the usual Kronecker delta.

To account for a half-space, the complementary terms $u_{ij}^C$ and $t_{ij}^C$ as well as the extra terms $u_{ij}^E$ and $t_{ij}^E$ are included such that (see Phan-Thien (65))

$$u_{ij}^* = u_{ij}^K - u_{ij}^C + u_{ij}^E \quad \text{and} \quad t_{ij}^* = t_{ij}^K - t_{ij}^C + t_{ij}^E \tag{14}$$

where

$$u_{ij}^K = \frac{1}{8\pi\mu}\left(\frac{\delta_{ij}}{R} + \frac{R_i R_j}{R^3}\right) \quad \text{and} \quad t_{ij}^K = -3\frac{R_i R_j R_m n_m}{4\pi R^5} \tag{15}$$

$$u_{ij}^E = \frac{X_3}{4\pi\mu R^3}\left\{ \delta_{j3}R_i + \delta_{i3}R_j - 2\delta_{i3}\delta_{j3}R_3 + x_3\left[2\delta_{i3}\delta_{j3} - \delta_{ij} + 3\frac{R_i}{R^2}(R_j - 2\delta_{j3}R_3)\right]\right\} \tag{16}$$

$$t_{ij}^E = -\frac{X_3}{2\pi R^5}\left\{ 3\delta_{j3}R_i R_m n_m - 3R_3 n_i(2\delta_{j3}R_3 - R_j) - 3x_3\left\{ \delta_{ji}R_m n_m + R_i n_j - 2\delta_{j3}(\delta_{i3}R_m n_n + R_i n_3) + \left(5\frac{R_i R_m n_m}{R^2} - n_i\right)(2\delta_{j3}R_3 - R_j)\right]\right\} - 2\delta_{j3}(\delta_{i3}R_m n_n + R_i n_3) + \left(5\frac{R_i R_m n_m}{R^2} - n_i\right)(2\delta_{j2}R_3 - R_j)]\right\} \tag{17}$$

and $\mathbf{R} = \mathbf{x} - \mathbf{X}^*$ (see Fig. 1). The complementary terms are identical to those of the Kelvin solution, except that the Stokeslet is taken at the point $\mathbf{X}^*$ (rather than $\mathbf{X}$), which is the reflection of $\mathbf{X}$ about the half-space.

## APPENDIX 2: DISCRETIZATION SCHEMES

The primary nodes, needed to define the vertices of the triangular elements, on the sphere of radius $a$ and center (0, 0, 0), are generated by beginning with the vertices of the relevant octahedron:

$$(\pm a, 0, 0), \qquad (0, \pm a, 0), \qquad (0, 0, \pm a).$$

By extending the midpoint of each edge to the surface of the sphere, the remaining necessary 12 vertices are found to be

$$\left(0, \pm\frac{a}{\sqrt{2}}, \pm\frac{a}{\sqrt{2}}\right), \qquad \left(\pm\frac{a}{\sqrt{2}}, 0, \pm\frac{a}{\sqrt{2}}\right), \qquad \left(\pm\frac{a}{\sqrt{2}}, \pm\frac{a}{\sqrt{2}}, 0\right).$$

The extra midside nodes are found in much the same manner. With minor appropriate alterations for radius and center, this scheme is employed above to discretize the spheres (The Motion of a Sphere Near Plane Boundaries) as well as the spherical cell bodies elsewhere.

Each point on the flagellar surface is considered to lie on the perimeter of a cross-sectional circle. All such circles are centered about the flagellar centerline, which is given by Eq. 4, and have the same radius (except very near the ends, where the radius decreases sharply to zero). Based on this idea, the equation defining the coordinates of every point on this surface may be derived for a given centerline geometry. Such an equation was given by Phan-Thien et al. (34), and the relevant procedure was discussed in greater detail by Ramia and Phan-Thien (66). The length of the flagellum is discretized into $n_f$ segments, by considering a finite number of cross-sections, which are in turn discretized into polygons of $\nu_f$ sides. These polygons are then used to model the entire flagellar surface by a series of, for example, pentagonal cylinders (for $\nu_f = 5$). The end segments are sealed by hemispherical domes consisting of $\nu_f$ trilateral and $\nu_f$ quadrilateral elements. Finally, an extra node is generated on each edge through which both adjacent quadratically curved elements are made to pass. This scheme, together with the 32 elements and their associated 66 nodes on the cell body, leads to a total of $M$ boundary elements and $N$ vertices, which are given by

$$M = N_o[(n_f + 4)\nu_f + 32]$$

and

$$N = N_o[(3n_f + 10)\nu_f + 68] \tag{18}$$

where, as previously defined, $N_o$ is the number of organisms considered. Throughout the present study, $n_f = 20$ and $\nu_f = 3$ (for all calculations), as shown in Fig. 5, which leads to 104 elements and 278 nodes for each organism.

As shown in Fig. 2, the circular plate is discretized into $n_p$ radial divisions and $\nu_p$ equal angular divisions. The width (in the radial direction) of the radial divisions is incremented, from the center outward, in a geometric progression with common ratio $c_r$. This ensures a greater density of elements at the center of the plate, in the vicinity of the organism (or other body such as the sphere or slender rod considered above in Boundary Element Method). The two sides of the plate are discretized in an identical manner, and the plate is given a

thickness of 1% of the plate radius. For the section above (The Motion of a Sphere Near Plane Boundaries) a plate radius of 15 is used, and the sphere radius is maintained constant at 1. Also above (The Motion of a Slender Body Near Plane Boundaries) the plate radius is taken to be 300, the rod's length $2l_f$ is 100, and its cross-sectional radius $a_f$ is 1. For the latter case (i.e., The Motion of a Slender Body Near Plane Boundaries), a typical set of calculations was repeated for a plate radius of 600, and the resulting differences were typically less than 1%.

## APPENDIX 3: DISCRETIZATION ERRORS

The following were identified as typical cases most likely to introduce the greatest discretization errors:

- swimming parallel and "close" to a half-space
- swimming perpendicular and "close" to a half-space
- two organisms swimming "close" and parallel to each other
- a single organism swimming parallel to, midway between, and "close" to two parallel plates

where the term "close" is used to imply a normalized minimum separation distance of zero (i.e., $s = 0$ as defined by Eq. 12).

For each of the first three of the above cases, three different discretization schemes were considered; fine, medium, and coarse. Using the fine discretization scheme as the standard, the percentage errors in the instantaneous linear velocity **U**, angular velocity $\boldsymbol{\Omega}$, propulsive force **F**, and propulsive torque **T**, due to each of the medium and coarse schemes were calculated (the instant with $\theta = 0$ was considered). The medium discretization scheme, which is employed for all the present calculations, consistently yielded errors of less than 0.5%.

The last of the above four cases is the most serious since it introduces an additional source of error, namely, that due to the finite size of the discretized plate. To quantify this source of error, the effect of the plate radius was investigated. In addition, the swimming of an organism inside a large thin flat fully enclosed cylinder (much like a coin) is considered. This latter approach proved to be very expensive computationally, because nodes on both the top and bottom plate as well as on their enclosing side walls constitute colocation points and will therefore necessarily be part of the solution process. A summary of the resulting errors, using a case with a finely discretized plate near a half-space as the standard, is given in Table 1, where

- Case 1 uses a plate with a radius of 20 and a medium discretization ($n_p = 15$, $v_p = 16$, and $c_r = 1.2$) near a half-space (similar to the cases depicted in Figs. 3*a*, 3*b*, 4*a*, and 4*b*).
- Case 2 uses a plate with a radius of 40 and a medium discretization ($n_p = 15$, $v_p = 16$, and $c_r = 1.4$) near a half-space (this is the actual discretization employed for all other calculations).

**TABLE 1 Convergence data for swimming parallel to and midway between two parallel plates**

| Quantity | Results Case 4 | Percentage differences Case 1 | Case 2 | Case 3 |
|---|---|---|---|---|
| $U_x$ | −0.018781 | 0.151 | 0.114 | 1.098 |
| $U_y$ | −0.008274 | 1.223 | 1.816 | 2.885 |
| $U_z$ | −0.069507 | 0.925 | 0.947 | 0.676 |
| $U$ | 0.07247 | 0.981 | 1.071 | 1.220 |
| $\Omega_x$ | 0.004201 | 0.068 | 0.027 | 0.093 |
| $\Omega_y$ | −0.023527 | 0.266 | 0.271 | 0.018 |
| $\Omega_z$ | 0.373722 | 0.230 | 0.181 | 1.847 |
| $\Omega$ | 0.373954 | 0.238 | 0.189 | 1.847 |
| $F_x$ | −0.684455 | 1.123 | 1.161 | 0.904 |
| $F_y$ | −1.377257 | 1.252 | 1.050 | 3.000 |
| $F_z$ | −7.782721 | 1.374 | 1.332 | 2.882 |
| $F$ | 7.933238 | 1.015 | 1.008 | 3.306 |
| $T_x$ | −1.653569 | 0.681 | 0.577 | 0.636 |
| $T_y$ | −0.465223 | 0.042 | 0.004 | 0.211 |
| $T_z$ | 38.38435 | 0.574 | 0.614 | 2.569 |
| $T$ | 38.42346 | 0.542 | 0.587 | 2.598 |
| Plate radius | 40 | 20 | 40 | 40 |
| $N$ | 1,599 | 999 | 999 | 1,832 |
| CPU time (s) | 15,265 | 4,990 | 4,990 | 24,526 |

- Case 3 uses a large thin flat fully enclosed cylinder of radius 40 and a medium discretization ($n_p = 15$, $v_p = 16$, and $c_r = 1.3$, which represents the maximum number of colocation points allowed by computational feasibility).
- Case 4 uses a plate with a radius of 40 and a fine discretization ($n_p = 22$, $v_p = 20$, and $c_r = 1.2$, which leads to approximately twice as many elements on the plate) near a half-space. This is used as a standard for calculating errors.

In all cases the same discretization scheme, with 278 nodes and 104 elements, was used for the organism.

For the actual case used (case 2), the maximum error is less than 2%, relating to the radial component of velocity $U_y$, which is small compared with the axial component $U_z$. This error reduces to $\approx$1% when the magnitude $U$ of the velocity, which is of primary concern here, is considered. Similar or smaller errors result for the magnitudes of other quantities, namely, $\Omega$, $F$, and $T$. The results for case 2, which has the same plate radius as the standard case 4, are proof that the error due to the plate discretization is acceptably small. The similar results for case 1, which has a much smaller plate radius than cases 2 and 4, indicate that the errors due to the finite size of the plate are also acceptable. Furthermore, the errors due to the open ends of the plate are shown to be equally small via the results for case 3, which employs a fully enclosed large thin flat cylinder to model the two plates.

## APPENDIX 4: CELL BODY/FLAGELLAR SEPARATION

As mentioned in Instantaneous Velocities (above), to assemble the elements of the resistance matrix in Eq. 6, the cell body and the flagellum must be considered as two separate bodies for each organism. Ideally, two such bodies should be made to touch (at a single point) but not overlap with each other. This would lead, however, to a singular system of equations (resulting from Eq. 3). There exists a general and widely accepted criterion for this, namely, that the minimum separation distance between two neighboring discretized bodies must be of the same order as or larger than the minimum separation distance between any two colocation points on either body. Here, the effect of the minimum cell body/flagellar separation distance on the instantaneous velocity $\mathbf{U}$ and angular velocity $\mathbf{\Omega}$ of a single organism in an unbounded fluid was investigated. As this distance was varied from $a_f/10$ to $a_f$, differences of less than 0.2% in $\mathbf{U}$ and $\mathbf{\Omega}$ were predicted. This is not surprising because near the joining point, the flagellum lies essentially on the flagellar axis of rotation and hence does not contribute significantly to the propulsive force or torque. For all calculations, this distance is currently kept constant at $a_f/2$.

## REFERENCES


1. Berg, H. C., and R. A. Anderson. 1973. Bacteria swim by rotating their flagellar filaments. *Nature (Lond.)* 245:380–382.
2. Meister, M., S. R. Caplan, and H. C. Berg. 1989. Dynamics of a tightly coupled mechanism for flagellar rotation. *Biophys. J.* 55:905–914.
3. Stewart, R. C., and F. W. Dahlquist. 1987. Molecular components of bacterial chemotaxis. *Chem. Rev.* 87:997–1025.
4. Berg, H. C., and L. Turner. 1990. Chemotaxis of bacteria in glass capillary arrays. *Biophys. J.* 58:919–930.
5. Crenshaw, H. C. 1993. Orientation by helical motion: Part 1. Kinematics of the helical motion of organisms with up to six degrees of freedom. *Bull. Math. Biol.* 55:197–212.
6. Crenshaw, H. C. 1993. Orientation by helical motion: Part 3. Microorganisms can orient to stimuli by changing the direction of their rotational velocity. *Bull. Math. Biol.* 55:231–255.
7. Crenshaw, H. C., and L. Edelstein-Keshet. 1993. Orientation by helical motion: Part 2. Changing the direction of the axis of motion. *Bull. Math. Biol.* 55:213–230.
8. Baba, S. A., S. Inomata, M. Ooya, Y. Mogami, and A. Izumi-Kurotani. 1990. Three-dimensional recording and measurement of swimming paths of microorganisms with two synchronized monochrome cameras. *Rev. Sci. Instrum.* 62:540–541.
9. Myerscough, M. R., and M. A. Swan. 1989. A model for swimming unipolar spirilla. *J. Theor. Biol.* 139:201–218.
10. Brennen, C., and H. Winet. 1977. Fluid Mechanics of propulsion by cilia and flagella. *Annu. Rev. Fluid Mech.* 9:339–398.
11. Taylor, G. I. 1952. The action of waving cylindrical tails in propelling microscopic organisms. *Proc. R. Soc. Lond. A* 211:225–239.
12. Taylor, G. I. 1951. Analysis of the swimming of microscopic organisms. *Proc. R. Soc. Lond. A* 209:447–461.
13. Reynolds, A. J. 1965. The swimming of minute organisms. *J. Fluid Mech.* 23:241–260.
14. Blake, J. R. 1971. Infinite models for ciliary propulsion. *J. Fluid Mech.* 49:209–222.
15. Smeltzer, R. T. 1972. A low Reynolds number flow problem with applications to spermatozoan transport in cervical mucus. M. S. Thesis. Massachusetts Institute of Technology, Cambridge, MA.
16. Katz, D. F. 1974. On the propulsion of microorganisms near solid boundaries. *J. Fluid Mech.* 64:33–49.
17. O'Brien, R. W. 1981. The gliding motion of a bacterium: *Flexibacter strain BH3. J. Aust. Math. Soc. B* 23:2–16.
18. Hancock, G. J. 1953. The self propulsion of microscopic organisms through liquids. *Proc. R. Soc. Lond. A* 217:96–121.
19. Higdon, J. J. L. 1979. A hydrodynamic analysis of flagellar propulsion. *J. Fluid Mech.* 90:685–711.
20. Higdon, J. J. L. 1979. The generation of feeding currents by flagellar motions. *J. Fluid Mech.* 94:305–330.
21. Higdon, J. J. L. 1979. The hydrodynamics of flagellar propulsion: helical waves. *J. Fluid Mech.* 94:331–351.
22. Lapage, G. 1925. Notes on the Chanoflagellate, *Codosiga botrytis, Ehrbg. Q. J. Microsc. Sci.* 69:471–508.
23. Sleigh, M. A. 1964. Flagellar movement of the sessile flagellates: *Actinomonas, Codonosiga, Monas* and *Poteriodendron. Q. J. Microsc. Sci.* 105:405–414.
24. Gueron, S., and N. Liron. 1992. Ciliary motion modeling, and dynamic multicilia interaction. *Biophys. J.* 63:1045–1058.
25. Sleigh, M. A., J. R. Blake, and N. Liron. 1988. State of art: the propulsion of mucus by cilia. *Am. Rev. Respir. Dis.* 137:726–741.
26. Gray, J., and G. J. Hancock. 1955. The propulsion of sea-urchin spermatozoa. *J. Exp. Biol.* 32:802–814.
27. Lighthill, M. J. 1976. Flagellar hydrodynamics: the John von Neumann Lecture 1975. *SIAM Rev.* 18:161–229.
28. Chwang, A. T., and T. Y. Wu. 1971. A note on the helical movement of microorganisms. *Proc. R. Soc. Lond. B* 178:327–346.
29. Shreiner, K. E. 1971. The helix as a propeller of microorganisms. *J. Biomech.* 4:73–83.
30. Katz, D. F., and J. R. Blake. 1975. Flagellar motions near walls. *In* Swimming and Flying in Nature, Vol. 1. T. Y. Wu, C. Y. Brokaw, and C. Brennen, editors. Plenum Publishing Corp., New York. 173–184.
31. Katz, D. F., J. R. Blake, and S. L. Paveri-Fontana. 1975. On the movement of slender bodies near plane boundaries at low Reynolds number. *J. Fluid Mech.* 72:529–540.
32. Wakiya, S. J. 1958. *Res. Rep. Fac. Eng. Niigata Univ.* 7:1–14.
33. Happel, J., and H. Brenner. 1973. Low Reynolds Number Hydrodynamics. Noordhoff International Publishing, Leyden, the Netherlands.
34. Phan-Thien, N., T. Tran-Cong, and M. Ramia. 1987. A boundary element analysis of flagellar propulsion. *J. Fluid Mech.* 184:533–549.
35. Rikmenspoel, R. 1965. The tail movements of bull spermatozoa: observations and model calculations. *Biophys. J.* 5:365–392.
36. Leifson, E. 1960. Atlas of Bacterial Flagellation. Academic Press, Orlando, CA.
37. Ramia, M. 1991. Numerical model for the locomotion of spirilla. *Biophys. J.* 60:1057–1078.
38. Youngren, G. K., and A. Acrivos. 1975. Stokes flow past a particle of arbitrary shape: a numerical method of solution. *J. Fluid Mech.* 69: 377–403.
39. Bush, M. B., and R. I. Tanner. 1983. Numerical solution of viscous flows using integral equation methods. *Int. J. Numer. Methods Fluids*, 3:71–92.
40. Tran-Cong, T., and N. Phan-Thien. 1989. Stokes problems of multiparticle systems: a numerical method for arbitrary flows. *Phys. Fluids A* 1:453–461.
41. Kim, S., and S. J. Karrila. 1991. Microhydrodynamics: Principles and Selected Applications. Butterworth-Heinemann, Boston.
42. Banerjee, P. K., and R. Butterfield. 1981. Boundary Element Methods in Engineering Science. McGraw-Hill, New York. 138–167.
43. Brebbia, C. A., J. C. F. Telles, and L. C. Wrobel. 1984. Boundary Element Techniques: Theory and Application in Engineering. Springer-Verlag, Berlin. 177–236.
44. Bathe, K. J. 1982. Finite Element Procedures in Engineering Analysis. Prentice-Hall, Englewood Cliffs, NJ.
45. Lee, S. H., and L. G. Leal. 1980. Motion of a sphere in the presence of a plane interface part 2: an exact solution in bipolar co-ordinates. *J. Fluid Mech.* 98:193–224.
46. Tran-Cong, T., and N. Phan-Thien. 1986. Boundary element solution for

half-space elasticity or Stokes problems with no-slip boundary. *Comp. Mech.* 1:259–268.

47. Phan-Thien, N., D. L. Tullock, and S. Kim. 1992. Completed double layer in half-space: a boundary element method. *Comp. Mech.* 9:121–135.
48. Smoluchowski, M. 1911. On the mutual action of spheres which move in a viscous liquid. *Bull. Sci. Cracovie A* 1:28–39.
49. Faxén, H. 1924. Die Bewegung einer starren Kugel läng der Achse eines mit zahër Flüssigkeit gefüllen rohre ariv. *Ark. Matematik, Astronomi Fysik* 18:1–52.
50. Happel, J., and B. J. Byrne. 1954. Motion of a sphere in a fluid in a cylindrical tube. *Ind. Eng. Chem.* 46:1181–1186.
51. Brenner, H. 1962. Effects of finite boundaries on the Stokes resistance of an arbitrary particle. *J. Fluid Mech.* 12:35–48.
52. Tillet, J. P. K. 1970. Axial, and transverse Stokes flow past slender axi-symmetric bodies. *J. Fluid Mech.* 44:401–417.
53. Cox, R. G. 1970. The motion of long slender bodies in a viscous fluid. Part 1. General theory. *J. Fluid Mech.* 44:791–810.
54. de Mestre, N. J. 1973. Low Reynolds number fall of slender cylinders near boundaries. *J. Fluid Mech.* 58:641–656.
55. de Mestre, N. J., and W. B. Russel. 1975. Low Reynolds number translation of a slender cylinder near a plane wall. *J. Eng. Math.* 9:81–91.
56. Fulford, G. R., and J. R. Blake. 1983. On the motion of a slender body near an interface between two immiscible fluids at very low Reynolds number. *J. Fluid Mech.* 127:203–217.
57. Fulford, G. R., and J. R. Blake. 1983. Slender body theory in mucociliary transport. *In* Eighth Australasian Fluid Mechanics Conference, University of Newcastle, New South Wales, 28 November–2 December.
58. Tullock, D. L., N. Phan-Thien, and A. L. Graham. 1992. Boundary element simulations of spheres settling in circular, square and triangular conduits. *Rheol. Acta* 31:139–150.
59. Ramia, M., and D. L. Tullock. 1990. Microorganism locomotion: an application of fluid mechanics and kinematics. *In* Proceedings of the Fifth National Congress on Rheology, Melbourne, 27–29 June. Y. L. Yeow and P. H. T. Uhlherr, editors. Australian Society of Rheology and Department of Chemical Engineering, University of Melbourne, Parkville, Victoria, Australia. 95–98.
60. Keller, J. B., and S. I. Rubinow. 1976. Swimming of flagellated microorganisms. *Biophys. J.* 16:151–170.
61. Goldstein, H. 1950. The Kinematics of rigid body motion. *In* Classical Mechanics. Addison-Wesley Publishing Co., Ltd., London. 93–143.
62. Paul, R. 1981. Robot Manipulators: Mathematics, Programming and Control. MIT Press, Cambridge, MA.
63. Vincent, J., N. Phan-Thien, and T. Tran-Cong. 1990. Sedimentation of multiple particles of arbitrary shape. *J. Rheol.* 35:1–27.
64. Swan, M. A. 1982. Trailing flagellar rotate faster than leading flagella in unipolar cells of *Spirillum volutans*. *J. Bacteriol.* 150:377–380.
65. Phan-Thien, N. 1983. On the image system for the Kelvin-state. *J. Elasticity* 13:231–2352.
66. Ramia, M., and N. Phan-Thien. 1988. The motion of slender bodies in a viscous fluid (a boundary element approach). *In* Proceedings of the Tenth International Congress of Rheology, Sydney, 14–19 August. Vol. 2. P. H. T. Uhlherr, editor. Australian Society of Rheology. 193–195.